# Near-surface Nitrogen Vacancy Centers in Diamond

## Citation

Cui, Shanying. 2014. Near-surface Nitrogen Vacancy Centers in Diamond. Doctoral dissertation, Harvard University.

## Permanent link

## Terms of Use

# Share Your Story

# Near-surface Nitrogen Vacancy Centers in Diamond

A DISSERTATION PRESENTED
BY
SHANYING CUI
TO
THE SCHOOL OF ENGINEERING AND APPLIED SCIENCES

IN PARTIAL FULFILLMENT OF THE REQUIREMENTS
FOR THE DEGREE OF
DOCTOR OF PHILOSOPHY
IN THE SUBJECT OF
APPLIED PHYSICS

HARVARD UNIVERSITY
CAMBRIDGE, MASSACHUSETTS
SEPTEMBER 2014

# Near-surface Nitrogen Vacancy Centers in Diamond

## Abstract

The nitrogen-vacancy (NV) center is a point defect in diamond and has been championed as a promising solid-state artificial atom. NV center properties such as its bright luminescence, room-temperature optical readout of spin states, and long spin decoherence lifetime make it an excellent system for applications in quantum information processing, high sensitivity magnetometry, and biotagging. In all applications, near-surface NVs are desirable. However, it has been found that the favorable properties of the NV center are significantly diminished as the NV center nears the surface.

This dissertation presents efforts in understanding the effect of the surface on the luminescence of NV centers less than a wavelength of light from the surface. We use plasma assisted etching to, independently, change the surface termination and bring the NV closer to the surface. We find that treating the surface with $CF_4$ plasma results in a deposited polymerous fluorocarbon which helps stabilize nearby NVs. We propose using a downstream etcher to bring NVs closer to the surface, while minimizing damage and maintaining NV luminescence. Finally, we enhance emission of these near-surface NVs by coupling them into a hybrid diamond plasmonic cavity. The fabricated devices result in a measured Q of 170, higher than other previously fabricated diamond plasmonic devices.

# Contents

# Author List

The following authors contributed to Chapter 3: Lee Bassett, John Mamin, Daniel Rugar, David Awschalom, Evelyn Hu

The following authors contributed to Chapter 4: Andy Greenspon, Kenichi Ohno, Bryan Myers, Ania Jayich, David Awschalom, Evelyn Hu

The following authors contributed to Chapter 5: Tsung-li Liu, Xingyu Zhang, Jonathan Lee, Kasey Russell, Evelyn Hu

# Listing of figures

# Acknowledgments

It never fails to astound me how generous, giving, and intelligent my colleagues, mentors, and friends are. This Ph.D thesis would not have been possible without their support.

First and foremost, I want to thank my advisor, Evelyn Hu. I came to Harvard on a recommendation from my undergraduate advisor that Evelyn is "the best advisor one could ever have." I was not disappointed. I am so grateful for the independence and guidance Evelyn has provided me throughout the past five years. Her confidence and trust in me pushed me to achieve more and forced me to have confidence in myself. I always feel like Evelyn is always my biggest advocate, which is incredibly comforting. From her, I have learned to become a better presenter, writer, scientist, leader, and person. In addition, the personal connection we shared has always meant a lot to me. Her mentorship has been a truly irreplaceable portion of my Ph.D program.

I worked in Professor Angela Belcher's lab four years at MIT as an undergrad researcher. Angie was the first female professor I became acquainted with, and I was always, and still remain, in complete awe of her ability to juggle a renowned research group and a family life at home. She encouraged me and mentored me not only throughout my undergrad years, but also after I graduated. Angie will always be a role model and a source of great inspiration to me.

I would like to thank my committee members Professors Marko Loncar and Ron Walsworth. I enjoyed Marko's class on Optics and Photonics so much, I actually took it twice. Marko has always been open to collaborations, and I've had the fortune of

working with various members of his group. I thank Ron for inviting me to speak at his group meeting and for always being so willing to collaborate, and share results. I would also like to thank our QuASAR collaborators, Professors David Awschalom, Ania Bleszynski-Jayich, and Dan Rugar, for encouraging me to present with them at several DARPA grant reviews and for making me feel part of a team, contributing to science. I have learned so much from the team about collaborations and team work, and how to effectively present as a group.

There are several other mentors in who have shaped me into the person and researcher I am. While in Angie's group, I worked with Andrew Magyar for all four years. Andrew showed me how to be a researcher, taught me the science behind our work, and patiently put out my fires (literally). Whenever approached him about a failed experiment, he always responded with "hmm, that's interesting..." By seeing the way he tackled research, I learned to not take unexpected results as failures but as something intriguing. It is because of our time in the Belcher lab that I decided to go apply for graduate school and continue research. I was fortunate to also have Andrew around as a post-doc in Evelyn's lab. From these two data points, I expect Andrew to apply for a job at HRL next (I'm waiting!)

When I arrived at Harvard, I was the only first year student to join Evelyn's new group (she had just moved from Santa Barbara). I found the senior members of the group incredibly intimidating. Luckily, this group bonded immediately and I owe so much of my small shred of sanity during the first three years of my Ph.D to them. Their excitement for science was infectious and uplifted me through my darkest and most doubt-filled moments. Kasey and Tsung-li rescued me from my constant rotation of projects not relevant to the group (Quantum dot solar cells! Biominizeralization with peptides! Self-assembly of who-knows-what!) and took me under their wings on the plasmonic project. It was because of their guidance, and their quiet, patient way of explaining fundamental physics that I finally started feeling part of the academic world. Kasey is an amazing scientist, writer, and person, with endless knowledge and new ideas. Even after Kasey left the group to pursue his start-up, he put aside many hours before or after a full day at work to consult me on my simulations or to simply calm my bewildered and frantic nerves, especially in the final few weeks

of writing this thesis. Also thanks to Kasey, I learned python, which is potentially the only practical skill gained in my Ph.D. Tsung-li was endlessly generous with his time, always willing to answer my questions about physics (of which, I'm convinced, he knows *everything* about) or to crawl around a dirty lab floor looking for lost diamond substrates (this happened multiple times). In addition to enlightening me about science and our project, he was always encouraging me when I didn't believe in myself. I owe much of this thesis to him. My only regret is not convincing him to change his gmail username. John Joo and I immediately bonded over mohawks, phage display, and a knack for "that's what she said" jokes. John was the glue of the Hu group, impossible to dislike and always a team player. John was also a hugely vital part of my PhD for his personal support and for lending a listening ear. Free coffee and sliding glass doors will never be the same again. Jonathan Lee was vital in helping me transition into my diamond project, on which I finally settled and wrote this thesis about. Jonathan also shattered my world when I found out he is not, in fact, Korean.

I was blessed with many other fantastic people in our group, an amazing cohort of quirky, funny, and smart people: Nan Niu (let it be known, in my Ph.D thesis, that you still owe me a Pusheen plush toy), Alex Woolf, Igor Aharanovich, Christine Zgrabik, Katie Greenberg, David Bracher, Andy Greenspon, Xingyu Zhang, Danqing Wang. I treasure all the memories of us chatting and eating lunch around a table that's too small before someone really awesome secured a table that is just the right size. Thank you each for all the times we spent reading my papers or thesis chapters, and for listening to and providing feedback on my practice talks. I've had the great fortune of working with insightful collaborators who were always willing to help: Kenichi Ohno, Paolo Andrich, Lee Bassett, Bryan Myers, and Dr. John Mamin. I am always amazed by smart everyone else is at Harvard, and have benefited much from helpful discussions with Anna Shneidman, Marc Warner, Birgit Hausmann, Jennifer Choy, Brendan Shields, Yinan Zhang, Mikhail Katz, Jonathan Fan, Raji Shankar, Young-Ik Sohn, Di Wei, Mike Burek, and Srujan Meesala. All of them, and many others whose name I did not list, also became my close friends. I had the great fortune to be part of a great community in the Harvard Graduate Women in Science

and Engineering (HGWISE). The executive board in particular has been a group of women I've grown very close to. There are plenty of people's names I have missed, but anyone who has ever shared a beer with me or fought me for a slice of that free pizza has contributed to this thesis. I am so grateful for all the support my friends within and outside Harvard have provided me in these years.

Finally, I would like to thank my family. My parents raised me to be inquisitive and to stay ambitious and goal-oriented. What they have given up and endured to provide me the privileged life I received is not possible to explain in a few sentences. Their love, pride, and support through all that I do gives me comfort nothing else in life can replace. Thank you to Jim, Ruth, Sarah, and Stephen for being my east coast family, and for your continued support and love. Thank you Jillian Dempsey and Alex Miller for being my big-siblings in graduate school, from helping me write my grad school and fellowship applications to listening to and giving feedback on my practice job talks.

Lastly, I would like to thank my fiancé Mike Miller. He is my rock, and has been with me through every step starting freshman year of college. I thank Mike for sharing everything with me these past nine years: frustrations, joys, scientific curiosity, and his french fries. He has read and edited just about everything I have ever written (any time you see a semicolon in this thesis, consider that Mike's "contribution.") Mike has always believed in me more than I ever believed in myself, and pushes me to achieve more. I am a stronger and better person because of him. I cannot wait to see what our future brings.

# 1

## Introduction

Diamond is a truly exceptional material, known for its extreme hardness and high thermal conductivity. It is optically transparent and can host hundreds of different point defect centers, called color centers, that emit light.[30] The nitrogen-vacancy (NV) center – one of the most well-studied centers – emits in the visible regime. Its unique spin properties allow it to act as a solid-state "artificial atom."[24] NVs have

generated much excitement around their applications in quantum information;[6] magnetometry;[27,3] nanoscale nuclear magnetic spin resonance spectroscopy (NMR)[78,50] and biosensing and marking.[23]

Several challenges stand in the way of realizing these applications. First, the desirable optical and spin properties of near-surface NVs—a necessity for almost all applications of NVs—are hampered by proximity to the diamond surface. Second, the collection of NV emission in air is inefficient due to the high dielectric constant of diamond. This thesis details our research toward both stabilizing and maximizing the radiation of NVs within the top 20 nm of the surface. To achieve these goals, we studied the effects of surface chemistry and subsurface damage on NV emission. We also designed and fabricated a diamond structure to enhance the collection of near-surface NV emission at a specific frequency.

This chapter provides an overview of the surface properties of diamond; the optical and spin properties of NVs; the desirability of near-surface NVs specifically and their applications. Finally, we demonstrate the need to better understand how diamond surfaces affect NVs.

## 1.1 Bulk diamond material properties

Diamond is a carbon allotrope made up of $sp^3$ bonds arranged in a unique diamond cubic lattice structure [Fig. 1.1]. The crystal consists of two interspersed face-centered cubic Bravais lattices where the four nearest neighbors form a tetrahedral geometry. These strong covalent bonds give rise to diamond's structural hardness. Diamond is chemically inert and resistant to most acids and bases. Diamond's high thermal conductivity also makes it a great heat sink material.



0,15 nm
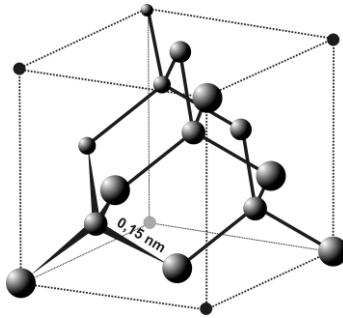
**Figure 1.1:** Diamond cubic lattice

Diamond is an electronic insulator with a wide band gap of 5.45 eV,[18] making it optically transparent in the visible regime. It can be doped with boron to become a p-type semiconductor. Due to the robustness of diamond, its boron-doped counterpart is often used as an electrode for electrochemical applications. Attempts to n-type dope diamond with a high density of nitrogen results in a donor state 1.7 eV from the conduction band.[18] This dopant level, however, is too deep to promote electrons into the conduction band. N-type doping of diamond remains elusive.

### 1.1.1 Diamond surface

Single-crystal diamond is grown homoepitaxially on another single-crystal diamond. Heteroepitaxial growth on cubic boron nitride (c-BN) or $\beta$-type silicon carbide ($\beta$-SiC) result in oriented, polycrystalline diamond.[18] Diamond growth is achieved with chemical vapor deposition (CVD), often in a mixture of $H_2$ and $CH_4$ gases. It is most commonly grown in a (100) orientation, as opposed to (110) or (111), to minimize the occurrence of grain boundaries.[62]

As is the case with all crystals, the surface can form in various configurations called surface reconstructions. These surface reconstructions minimize the surface energy and limit dangling bonds. Which surface reconstruction forms depends on the chemical bonding of the top few lattice sites. Figure 1.2 illustrates a cross-section of geometry for (100) surfaces before and after reconstruction. These configurations affect the energy and reactivity of diamond at the surface.

For a carbon-terminated diamond surface, an unreconstructed (100) surface has two dangling bonds (represented by the dotted red lines in figure 1.2a). Such a surface prefers to relax to a 2x1 geometry, where neighboring surface atoms form $\pi$-bonded dimers, similar to a cleaved (100) Si surface[68] [Fig. 1.2b].

An idealized carbon-terminated surface is not practically feasible. Since diamond is grown in the presence of $H_2$ gas, a hydrogenated surface is commonly seen. Hydrogen-termination reconstructs to a (100)2x1:2H surface, where the $\pi$-bond between the dimers is replaced by a covalent bond to one hydrogen[62] [Fig. 1.2d]. The (111) and (110) surface reconstruct to 1x1:1H and 1x1:2H, respectively. Hydrogen atoms can be desorbed by annealing the substrate to 900 - 1000°C in vacuum. The
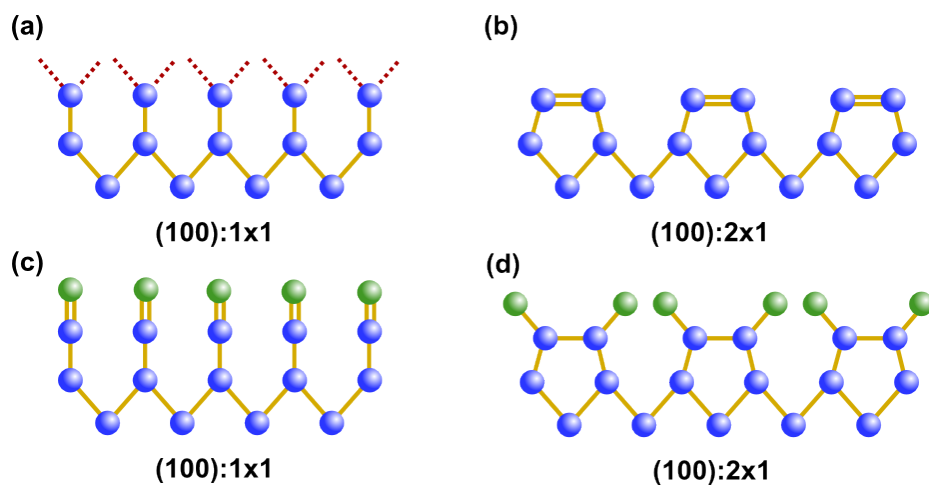
**Figure 1.2:** Cross-sectional schematic of the top three atoms of an ordered (100) diamond in a 1x1 geometry (a,c) and a 2x1 geometry (b,d). The fourth carbon bond is not shown. Blue spheres represent carbon atoms and green spheres represent non-carbon termination atoms or groups. Dashed red lines represent dangling bonds."

surface then readjusts to find the minimum energy configuration for a bulk-terminated surface.[62,82]

A diamond cleaved or left out in air is oxygen-terminated. Unlike hydrogen, carbon and oxygen can bind in a variety of different chemical compositions. A ketone (C=O) configuration relaxes to a (100)1x1 surface [Fig. 1.2a], whereas ether (C-O-C) and hydroxyl (C-OH) groups relax to a (100)2x1 reconstruction[49] [Fig. 1.2d]. Hydroxyl-termination (C-OH) is also possible with a (100)1x1 surface. Oxygen similarly desorbs from the surface after the diamond is heated above 900°C[49] in vacuum.

All these reconstructions assumes a perfectly sp$^3$-bonded structure. Ion implantation, physical sputtering, and annealing, however, may break some sp$^3$ bonds. If a sufficient number of sp$^3$ carbons are broken, graphitization occurs. The resulting sp$^2$-bonded carbons drastically change the electrical and optical properties of the diamond. The surface is relatively stable when annealed up to 1800°C in vacuum and

800°C in $O_2$.[18] Above these thresholds, the surface forms a graphitized layer that then burns off rapidly. This process effectively etches the diamond.

## 1.2   Nanodiamonds

Due to the chemical inertness of diamond, there is interest in using nanodiamonds in biological systems as robust fluorophores and local probes of magnetic field or spin.[36] Nanodiamonds share many similarities with bulk diamonds, only with a higher surface-to-volume ratio. Oxygen-terminated nanodiamonds are hydrophillic and can be easily suspended in aqueous solutions.

Nanodiamonds were first discovered in the 1960s by detonating bulk diamonds in a closed chamber.[37] These "detonation diamonds" were generally 4-5 nm in size but covered with graphitic soot. While relatively cheap to manufacture, these nanodiamonds have a high $sp^2/sp^3$ ratio. Furthermore, they aggregate easily and are difficult to disperse evenly onto a surface.

Grinding large CVD-grown crystals down to particles between 5 and 100 nm in diameter produces a purer form of nanodiamond. Alternatively, nanodiamonds can be grown in a CVD reactor with small diamond slurries as seeds. Nanodiamonds produced by either of these methods are single-crystal with jagged edges.[29]

Using nanodiamonds for pH-tunable drug release or targeted biomarking requires chemical functionality at the surface.[36] Small linker molecules can covalently bind to certain surface functional groups, such as carboxylic acids or alcohols. These linker molecules can then bind to antibodies or proteins. Functionalization can also be achieved by taking advantage of surface electrostatics. An oxidized surface, for

instance, is slightly negatively charged and will bind to a positively charged polymer. A layer-by-layer structure of alternating negatively and positively charged polymers can result in a fully coated nanoparticle. The polymers can be shed in solution by simply adjusting the pH.

## 1.3 Surface conductivity and electronic band structure

In 1989, Landstrass and Ravi discovered that undoped diamond—always considered to be purely an insulator—could become conductive after the surface is hydrogenated.[39] The mechanism for this conduction, however, was unknown at the time. This conduction was later proposed to arise from a *p*-type surface conductive layer, confined to the first 10 nm of the surface, with an activation energy of around 50 meV,[18] almost an order of magnitude less than the acceptor level of boron dopant.[18] We currently believe the conductivity stems from a combination of the electron affinity at the surface and electron acceptors in surface adsorbates.[48]

The structure and chemistry of the surface dictates the band pinning and bending of the material in relation to the vacuum level. Electron affinity (the minimum energy required to eject an electron) depends on the surface dipole, which can be engineered by changing both the surface termination (e.g., hydrogen or oxygen) and the reconstruction pattern. For an insulator, that is equivalent to the energy between the conduction band and the vacuum level. *Ab initio* density functional theory (DFT) calculations have been used to determine the ionization potentials and electron affinities for different surfaces.[76]

For a hydrogen-terminated sample, a surface dipole arises from the carbon-hydrogen

bond at the surface. Hydrogen is less electronegative than carbon which leads to a negative electron affinity at the surface of diamond [Fig. 1.3a]. Experimental proof of the negative electron affinity was first found experimentally in 1994 by photoemission spectroscopy.[82]
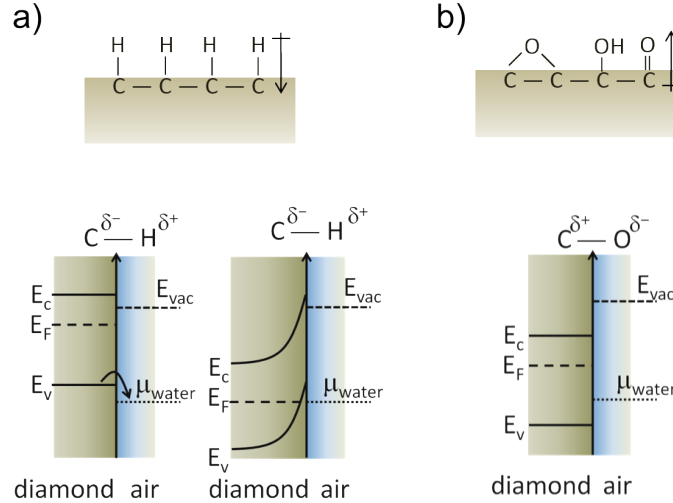


**Figure 1.3:** Schematic of surface chemistry (arrow signifies dipole direction) and electron affinities for an (a) hydrogen- and (b) oxygen-terminated diamond surface. Surface band bending in hydrogen-terminated surfaces results in surface conductivity.

Maier *et al.* proposed that the surface conductivity originates from a thin layer of water that is formed on the surface of the sample when exposed to the atmosphere. Because of hydrogenated diamond's negative electron affinity, the chemical potential of electrons in water ($\mu_{water}$) is lower energy than the diamond's valence band ($E_v$)[Fig. 1.3]. Electrons are transferred from the diamond to the water layer, driven by the redox reaction $2H_3O^+ + 2e^- \rightleftharpoons H_2 + 2H_2O$. This electron transfer causes the surface bands to bend upwards, resulting in hole accumulation at the surface. The Fermi level is thus pinned 50 meV below the valence band and the surface becomes conductive. According to the Nernst law, $\mu_{water}$ changes with pH. Hence, the

conductivity of the diamond depends on the pH of the water layer. Lower pH leads to higher conductivity as $H^+$ ion concentrations in the water layer increase.[53] This theory was further confirmed by annealing in ultra-high vacuum at temperatures between 200°C and 450°. This process causes the water and adsorbed ions to leave the surface, without breaking the carbon-hydrogen bonds. As a result, the surface maintains the negative electron affinity but no electron transfer to the water layer occurs and no surface conductivity is observed. When the sample is returned to atmosphere, conductivity is restored.[69]

In contrast, in an oxygen-terminated surface, because oxygen is more electronegative than carbon, the C-O surface dipole points in the opposite direction of the C-H dipole [Fig. 1.3b]. This orientation results in a positive electron affinity for the diamond. The valence band has a lower energy than $\mu_{water}$ and the adsorbed $H_2O$ layer no longer acts as an electron acceptor. No significant band bending occurs.

Oxygen binding at the surface can dramatically affect electron affinity. For instance, the ether-terminated (1x1):O surface leads to positive electron affinity. By contrast, a hydroxyl-terminated surface (C-OH) leads to a negative electron affinity similar to a hydrogen-terminated surface. This hints at some issues such chemical variations at the surface could cause, which will be further explored in chapter 3.

## 1.4 Nitrogen-vacancy defects in diamond

The Nitrogen-Vacancy center (NV), one of many luminescent defects found in diamond, is a point defect consisting of a substitutional nitrogen atom next to a carbon vacancy, oriented along the (111) crystalline direction. The electronic transitions in

NVs are embedded in the band gap of diamond, away from both the valence and conduction bands. The NV is thus a deep-level defect, and its optical transitions are protected from thermal fluctuations at room temperatures. The NV center has excellent optical and spin properties, making it an exciting candidate for many applications ranging from acting as a stable fluorophore to magnetic sensing.

### 1.4.1 CHARGE STATES

NVs have been observed in two charge states: neutral ($NV^0$) and negative ($NV^-$).[14] The negative NV has six electrons and is paramagnetic whereas the neutral NV has five electrons. The relative concentrations of $NV^0$ and $NV^-$ centers in bulk depends on the concentration of donors (such as interstitial nitrogen, $N_s$) and acceptors (such as vacancies) within the lattice.[10] In type IIa diamonds, which have very small concentrations of $N_s$, there is a significant variation in the relative concentrations of the two charges.[14] The $NV^+$ is also theorized to exist but has yet to be detected.[75]

### 1.4.2 OPTICAL PROPERTIES

Both charges of NVs have been shown to be photostable even when excited off-resonance.[14] Unlike fluorescent dyes or colloidal quantum dots, prolonged exposure to laser light does not result in photobleaching (the gradual dimming and disappearance of luminescence). An incident 532 nm laser excites both $NV^0$ and $NV^-$, and reveals a photoluminescence spectrum composed of two sharp, electronic transitions at 575 nm and 637 nm respectively, as well as a broadband vibrational background [Fig. 1.4]. The purely electronic transition, called the "zero-phonon line" (ZPL), involves no

phonons. At room temperature, transitions assisted by diamond lattice vibrations give rise to a broad emission below the ZPL energy called a "phonon side band." When cooled, the phonon side bands become less prominent and the ZPLs sharpens considerably.
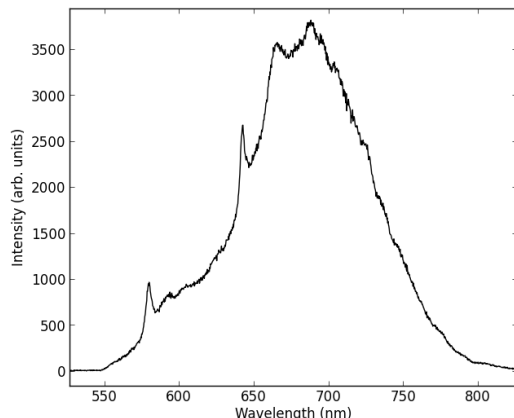


**Figure 1.4:** Nitrogen-vacancy photoluminescence at room temperature. $NV^0$ are $NV^-$ zero-phonon lines are at 575 and 637 nm, respectively.

The NV center is an efficient emitter, especially compared to most fluorescent dyes. The radiative quantum efficiency, defined as the fraction of radiative emission over total emission (radiative and non-radiative), is around 70-80% for NVs.[75] The radiative lifetime of $NV^0$ and $NV^-$ in bulk diamond is around 20 and 13 ns, respectively.[29] The radiative lifetime is considered to be temperature independent.[14] In nanodiamonds, $NV^-$ centers have a longer lifetime of 25 ns due to the decrease in effective refractive index of the medium surrounding the NV.[14]

While the internal quantum efficiency of an NV is high, the extraction of NV emission is great challenge. Due to the high refractive index (n=2.4) of diamond, much of the light emitted from an NV is totally internally reflected. The extraction

efficiency, calculated by the ratio of photons collected above the diamond to total photons emitted, is only around 3%.[26] Moreover, the branching ratio, defined as the fraction of light emitted into the ZPL over all frequencies, is also around 3% even at low temperatures.[16] For many applications of NVs that rely on $NV^-$ ZPL, most of the NV emission is considered wasted in the vibrational phonon side bands.

Nonetheless, the photostability of NVs, especially when embedded in nanoncrystals, makes them great candidates for broadband fluorescent labels and single-photon emitters.

### 1.4.3  SPIN PROPERTIES
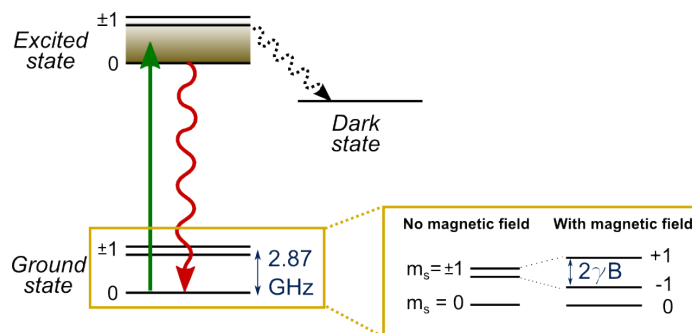


**Figure 1.5:** Electronic structure of $NV^-$ center.

A simplified electronic structure of the $NV^-$ center is shown in figure 1.5. The negatively-charged $NV^-$ state forms a spin triplet (s=1) in its ground state. An essential feature of the NV electron spin state is that it can be initialized, manipulated, and read out optically at room temperature. The $NV^0$ center, in contrast, has no detectable magnetic resonances. Because the $NV^-$ is the only charge with optical read-out of its spin, maximizing the $NV^-$ emission over $NV^0$ and $NV^+$ is crucial.

The crystal field splits the $m_s=0$ and $m_s = \pm1$ sublevels of the NV$^-$ ground state to be 2.87 GHz apart. Optical read out of spin is possible because electrons populated in the $m_s = \pm1$ level are 30% dimmer than electrons in the $m_s = 0$ state. Electrons excited from the $m_s = \pm1$ state are more likely to relax non-radiatively through a dark shelving state [Fig. 1.5]. Consequently, when a field induces a transition between the spin sublevels, a dip in detected NV photoluminescence can be seen. An example of the optically detected electron spin resonance (ESR) spectrum is shown in figure 1.6.
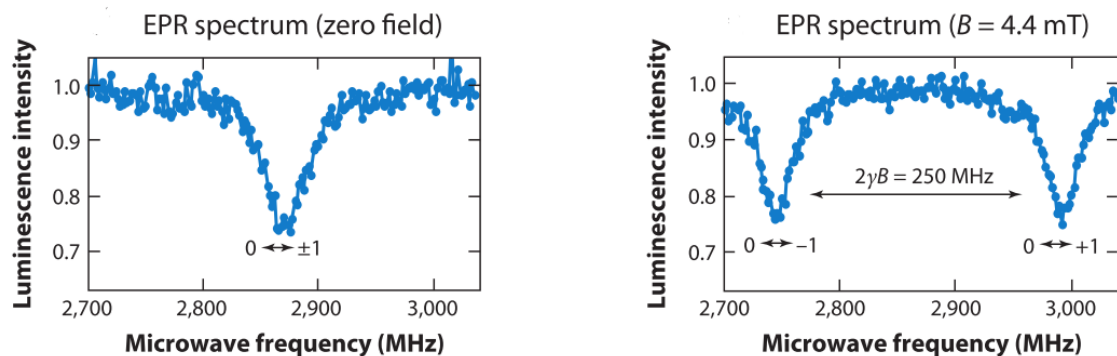


**Figure 1.6:** Electronic Spin Resonance (ESR), also known as Electronic Paragmentic Resonance (EPR) spectrum at no magnetic field, and in the presence of a magnetic field. Figure taken from 75.

In the presence of a magnetic field, the degeneracy of $m_s = \pm1$ spin sublevels is lifted by the Zeeman effect [Fig. 1.5]. The energy separation of the $m_s = +1$ and -1 levels equals $2\gamma B$, where $\gamma$ is the electron gyromagnetic ratio and B is the magnitude of the magnetic field parallel to the NV axis. Consequently, in the presence of a magnetic field, the ESR spectrum now shows two dips [Fig. 1.6]. This method is one of the most basic ways of sensing DC magnetic fields.

A more sensitive approach to sensing magnetic fields and spins relies on pulsed

experiments in a pump-probe scheme, where the NV spin evolves over a sensing period $(\tau)$. The magnetic field sensitivity is directly proportional to this evolution time. The maximum possible $\tau$ is set by the electron spin decoherence time, $T_2^*$, which is a result of spin-spin relaxation, such as coupling nuclear spins in the diamond lattice or surface electron spins. $T_2^*$ lifetime reflects how quickly a spin "forgets" the direction it was oriented in. Various schemes of pulse sequences have been proposed to decouple the spin from its environment to improve the measured $T_2$ lifetime. Coherence times as long as $T_2 \approx 2$ ms have been measured, which corresponds to AC magnetic field sensitivities of $\approx 10$ nT/Hz.[70] Such high sensitivity has enabled the detection of ensemble nuclear spin from protons.[50] However, the fundamental limit of $T_2$ still lies in the spin noise from paramagnetic impurities within the diamond lattice and surface spins.

## 1.5 CHALLENGES OF NEAR-SURFACE NITROGEN VACANCY CENTERS

One of the most exciting applications of the NV center is using it to sense external spin. Taking advantage of the angstrom size of the point defect, we can image nuclear spins on a nanometer scale. The sensitivity to external spins can be improved by longer $T_2$ times; increased detection of the NV zero-phonon line; and decreased distance of the NV to the diamond surface.

NVs must be placed close to the surface to achieve high magnetic sensitivity of external spins (ideally <5 nm). Proximity to the surface is important because a dipolar magnetic field falls off as $r^3$, where r is the distance of the NV to the source.[70] However, as the NV gets closer to the surface, $T_2$ lifetimes decrease and NV lumines-

cence gets less stable. It has been found that NVs implanted at shallow depths below 5 nm result in lowered $NV^-/NV^0$ ratios, significantly broadened ESR linewidths, and shortened $T_2$ decoherence lifetimes.[56] Furthermore, the photoluminescence of NVs less than 5 nm from the surface has been found to disappear and reappear suddenly, a phenomenon known as photoblinking.[4] One potential contribution to the near-surface NV fragility is the conversion of $NV^-$ to $NV^0$ or $NV^+$. Any imperfections in the diamond surface can result in dangling bonds which act as electron traps. And finally, as discussed earlier, different terminations result in surface band bending, which tend to favor $NV^0$.

Another way to increase magnetic sensitivity is to improve the optical collection of the NV ZPL. Only 3% of the collected light is from the $NV^-$ ZPL: most of the emission is wasted in the vibration phonon side bands, even at low temperatures. Moreover, only 3% of all photons are collected, due to the poor extraction efficiency. The solution for both the poor extraction efficiency and low branching ratio is shaping diamonds into photonic devices that trap light and enhance emission. Considerable progress has been made in enhancing NV ZPL emission.[2,7,73,40] However, creating these structures in diamond causes two problems. It increases the surface to volume ratio, thereby again bringing NVs close to the surface and reintroducing problems related to surface proximity. Secondly, these photonic devices require diamond to be etch-removed through plasma-assisted dry etching. Etching can cause permanent damage to the diamond lattice, creating vacancies and implanting unwanted defects. These subsurface damages adversely affect NV properties as well.

NV centers have great potentially for many applications, especially in the field

of nanomagnetometry. Manipulating the surface and stabilizing near-surface NVs pose considerable obstacles, however. The aim of this thesis is to study the effects of different surface treatments on NV charge and NV luminescence.

## 1.6 OVERVIEW

There are several surface properties of diamond that affect nearby nitrogen vacancy centers:

1. Distance from NV center(s) to surface

2. Chemistry and structure on surface

3. Subsurface environment: vacancy and contamination concentration

In order to understand their effects, it is important to decouple and address each surface property in isolation. The health of NVs can be assessed through the spin decoherence lifetime ($T_2$), the on-resonance ZPL linewidth, the $NV^-/NV^0$ ratio, and the overall NV brightness. In this thesis, we will be focusing primarily on the latter two properties, measured from the photoluminescence of ensemble NVs.

We begin by introducing the materials and methods used throughout the thesis in chapter 2. We will cover the different ways of incorporating NVs into diamonds, and how we analyze the surface chemistry and NV optical characteristics. We first study the effect of the surface in chapter 3, by addressing the effect of changing only the chemical termination of diamond surface. We measure the effect of different surface terminations on the $NV^-/NV^0$ ratio. Specifically, we discuss our work on stabilizing NV charge through a fluorocarbon polymer.

Chapter 4 explores the effects of bringing NVs closer to the surface with plasma etching. This chapter focuses on characterizing the potential damage that reactive ion etching induces on the subsurface environment. We study the overall NV luminescence as the diamond surface is slowly etched away in different reactors. We propose a system for minimizing damage to near-surface NVs.

Chapter 5 addresses the poor collection efficiency and low branching ratio of NVs. We design, fabricate, and measure an optical cavity that creates a region of high electric field close to the surface of diamond to enhance the emission of near-surface NVs. The proposed structure relies on the hybridization of a mode in a 2D photonic crystal in diamond with a silver substrate to create a gap mode.

Through all these chapters we study the effect that nanofabrication has on the surface chemistry of diamond and its subsequent effect on near-surface NVs. Our results will hopefully be of interest and assistance to researchers working on NV diamond devices for a variety of applications, and to others working on similarly sensitive materials with fabrication-intensive steps.

# 2

# Methods and Materials

In this thesis, the study of near-surface NVs and the effect of surface treatments follow a generalized experimental process: 1) create near-surface NVs, 2) change the surface, 3) analyze the surface chemistry and measure the NV emission. Most of our studies are done with bulk, single-crystal diamonds. The device in chapter 5, however, requires a much thinner diamond, so single-crystal diamond membranes

need to be lifted-off and processed. The materials, instruments, and methods used in all experiments are introduced here.

## 2.1 Nitrogen-vacancy creation in diamond

Diamonds mined from the earth have many natural color centers, including nitrogen vacancy centers (NVs). For our studies, it is important to have control over the NV density and distance from the surface. Moreover, we want to measure only the near-surface NVs. Thus, we need to start with a substrate that has virtually no detectable luminescent defects. We purchase the highest purity, chemical vapor deposition (CVD) grown, (100)-oriented electronic grade diamond (Element6). The concentration of nitrogen and boron are less than 5 ppb and 1 ppb, respectively. No NV luminescence was measured in these purchased diamond plates. NV centers can then be engineered and incorporated by ion implantation of nitrogen or during CVD overgrowth of the diamond.

### 2.1.1 Ion implantation
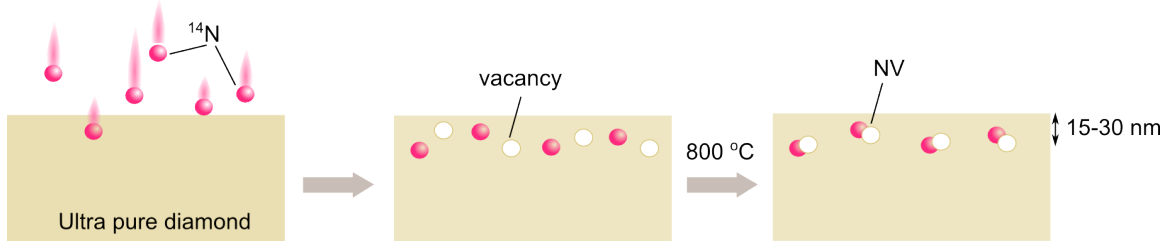


**Figure 2.1:** Ion implantation method of creating nitrogen-vacancy centers.

Ion implantation is a technique in which high energy ions are accelerated towards

a surface and incorporated into the lattice of the target material. The irradiation displaces a carbon atom from its original lattice position and creates a vacancy and an interstitial defect (Frankel pair) in the diamond lattice. Implanting with nitrogens generates several types of defects: interstitial nitrogen ($N_s$), divacancy ($V_2$), $N_2V$, $N_2$, and NVH.[10]
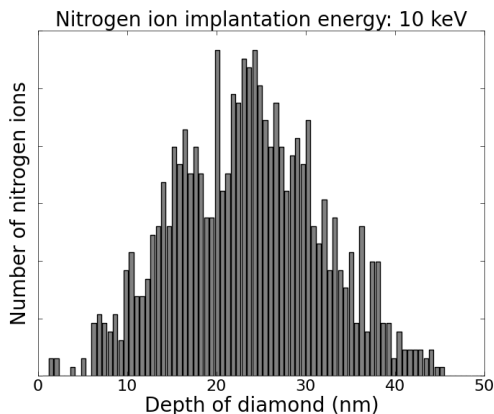


**Figure 2.2:** SRIM model showing ion implantation straggle.

To create near-surface NVs, we implant high-purity diamonds with Nitrogen-14 at 10 keV with varying densities [Fig. 2.1]. The depths of these defects depend on the incident energy of the implanted ions. We can approximate the depths with Stopping Range of Ions in Matter (SRIM) software. SRIM models the collisions of the incoming ions with the target material based on a Monte Carlo simulation. A SRIM model of nitrogens implanted into diamond at 10 keV is plotted in figure 2.2, showing an average depths of around 20 nm. The ion dosage is controlled by the concentration of ions / $cm^2$, which affects the density of $N_s$, and eventually the density of NV.

Next, we anneal our diamond at 800°C in vacuum for two hours to allow the vacancies to diffuse and meet with a substitutional nitrogen to create NVs. This an-

nealing step, along with the damage caused by ion implantation, creates a graphitized layer of primarily sp$^2$ C-C bonds at the surface of the diamond. Chapter 3 explores the effect of this layer on nearby NVs. A boiling triacid solution is used to remove the graphitic carbon as described in section 2.4.

Ion implantation is one of the most common ways to generate NVs. It is reliable, and many existing businesses offer implantation services with a turnaround time of only a few days. However, there are two major issues with ion implantation: damage and depth variance.

Ion implantations causes damage in the form of vacancies in the lattice and graphitization at the surface. In section 2.3, we take advantage of the sp$^2$ bonds to lift off thin membranes of diamond. The same technique does not apply well to our bulk diamond surfaces, creating an excess of vacancies and broken bonds. Chapter 4 discusses NV emission dimming and charge state switching as a result of these vacancies.

Ion implantation can produce NV with a significant variation in depth. According to figure 2.2, at our preferred implantation energy of 10 keV, NVs are most likely to be within 15 - 30 nm, but NVs can also be 5 or 45 nm deep. This is especially an issue in chapter 4, when we slowly etch-remove diamond to bring NVs closer to the surface: it is unclear if the NVs are dimming because of our processing or because we are etching away a significant number of near-surface NVs. We therefore need a sample where the NV layer is more confined and well-defined.

## 2.1.2 DELTA-DOPED SAMPLES

Our collaborators at UCSB, namely K. Ohno, have developed a technique, where NVs are incorporated during the CVD growth of diamond and are confined to depths only a few nanometers apart. This process, called "delta-doping" is described in more detail elsewhere.[58] The sample used in chapter 4 is grown on a purchased bulk, ultra pure diamond (Element6). First $50 \pm 20$ nm of $^{12}$C diamond is grown via plasma-enhanced chemical vapor deposition (PECVD). The actual growth rate can vary a fair bit, depending on the chamber conditions. Nitrogen is then incorporated during a short growth period by flowing in 10 sccm of $N_2$. Finally another $50 \pm 20$ nm of $^{12}$C buffer layer is grown on top. Vacancies are created by electron irradiation ($10^{12}$ cm$^{-2}$ dose at 7 keV). Finally, the sample is annealed at 850°C for 2 hours in $H_2$/Ar to diffuse vacancies into the N-doped layer. The uncertainty in the diamond growth rate means there is some uncertainty in the actual depth of the NVs from the surface ($z = 50 \pm 20$ nm). However, we know the straggle of the NVs ($\Delta z$) is only $\pm$ 4 nm. Hence, the NV layer is considered delta-doped. This sample has an estimated NV density of around 3.5 x $10^{14}$ cm$^{-3}$.

## 2.2 MASKING

Masks are used throughout to protect parts of the surface or to create an edge to measure the etch rate of an instrument. A silicon dioxide mask is created by first depositing 300 nm of silicon dioxide with PECVD. Photoresist (Shipley) is spin coated onto the $SiO_2$ layer and soft-baked at 115°C, and patterned with photolithography.

The pattern is transferred to the silicon dioxide layer by submerging the diamond in a solution of 5:1 buffered oxide etchant (BOE) for one minute and fifteen seconds. The photoresist mask is removed in acetone. Concentrated hydrofluoric acid (HF) is used to ultimately remove the $SiO_2$ mask.

## 2.3   CREATING DIAMOND MEMBRANES

As discussed earlier, ion implantation creates a graphitized, damaged layer. In this section, we take advantage of the damaged layer by using it as a lift-off point to create hundreds of nanometer-thin membranes, which will be used in the photonic devices discussed in chapter 5. More detail of the membrane fabrication and binding process can be found in Lee's PhD thesis.[41]
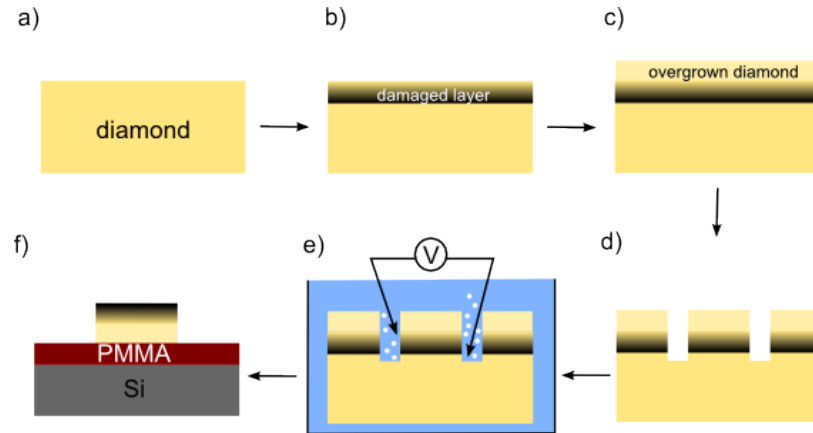


**Figure 2.3:** Fabrication of diamond membrane.

A bulk diamond is ion implanted with helium ions at 1 MeV to create a graphitized layer approximately 1.7 $\mu$m deep into the substrate [Fig. 2.3b]. Using the old substrate as a homoexpitaxial template, a pristine diamond layer is then overgrown in a CVD set-up by our collaborators in David Awschalom's or Ania Jayich's group at UCSB.

These overgrown layers can either consist of only diamond, or can incorporate NVs at engineered depths.

Next, we pattern 400 x 400 $\mu$m squares on the sample with a $SiO_2$ mask and use $O_2$ plasma in a reactive ion etcher (RIE) to etch $\approx 2\mu$m deep [Fig. 2.3d]. We then apply 12 V across the damaged region of the membrane in an aqueous solution to lift-off individual membranes. We bind each membrane (initially $\approx 1.4\mu$m thick) by pressing the membrane onto a silicon wafer with freshly spun poly(methyl methacrylate) (PMMA). The membrane is then baked into the PMMA layer at 180°C for 5 min, such that the membrane lies flat and is fixed into position. A combination of $Ar/Cl_2$ and $O_2$ plasma is used to etch off the damaged region created by the helium ion implantation. The etch step is important because the damaged region has a broadband luminescent background and results in unstable NVs. The final result is a thin layer of diamond $\approx 200$ nm thick, without any evidence of the damage caused by ion implantation.

## 2.4 SURFACE TREATMENTS

Various techniques are used to either change the surface termination, to etch-remove the diamond material, or to simply clean the surface. This section briefly introduces these techniques.

### 2.4.1 WET CHEMISTRY

The chemical termination of the diamond as discussed in section 1.1.1 is not affected by wet chemistry. The only exception is a high temperature solution of nitric, sulfuric,

and perchloric acid, which is used to both remove graphitic carbon at the surface and to oxygen-terminate the surface. In this process, we submerge the diamond in 1:1:1 $HNO_3$:$H_2SO_4$:$HClO_4$ within a round bottom flask. The flask sits on a heated sand bath and is attached to a condenser, cooled by 15°C water. The triacid solution is heated to its boiling point for two hours. We believe that the triacid clean may also etch the diamond, albeit very slowly. The exact rate is unknown because it also etches through most mask materials we might use to determine the rate.

To remove organic contaminates from the surface of diamond, a pirhana clean, 3:1 $H_2SO_4$:$H_2O_2$, is used. Pirhana does not always reliably oxygen-terminate the surface. Solvent cleans (e.g., acetone and isopropanol) and HF are also used to clean the surface, but were found to not affect the surface chemistry.

### 2.4.2 Plasma treatments

Plasma etching is used throughout both to change the surface termination and to etch the surface. Three main types of plasma etching systems are used: an inductively-coupled reactive ion etcher (ICP RIE) (Unaxis Shuttleline or STS); barrel reactor (Technics); and downstream etcher (YES or Matrix). An introduction to plasma reactors can be found in chapter 4.

The ICP RIE system creates a high-density plasma and applies a DC bias to accelerate the charged ions towards the surface. The chuck on which the sample sits is cooled to room temperature. The process conditions are listed below in table 2.1. Processes #1-2 are used to etch hundreds of nanometers of diamond. Processes #3-5 have been optimized to have low bias voltages and etch rates.

**Table 2.1:** ICP RIE processes

| # | Gas | Flow rate | Pressure | Chuck bias | Plasma power | Diamond etch rate |
|---|-----|-----------|----------|-----------|--------------|-------------------|
| 1 | $O_2$ | 20 sccm | 10 mT | 210 V | 600 W | 160 nm/min |
| 2 | $Ar/Cl_2$ | 40/25 sccm | 5 mT | 280 V | 500 W | 100 nm/min |
| 3 | $O_2$ | 20 sccm | 10 mT | 50 V | 600 W | 8 nm/30 sec |
| 4 | $H_2$ | 30 sccm | 3 mT | 60-100 V | 600 W | 1 nm/min |
| 5 | $SF_6$ | 20 sccm | 3 mT | 5-30 V | 600 W | <1 nm/min |

The Technics Micro-stripper 220 is a table-top RF plasma reactor with multiple gas supplies. The discharge to create the plasma is formed isotropically around the sample between rods that run along the length of the chamber. No bias voltage is applied.

**Table 2.2:** Technics Microstripper processes

| Gas | Flow rate | Base pressure | Plasma power | Diamond etch rate |
|-----|-----------|---------------|--------------|-------------------|
| $O_2$ | 25 sccm | 380 mT | 200 W | 0.1 nm / min |
| $SF_6$ | 56 sccm | 230 mT | 200 W | N/A |

Finally, in a downstream system, the plasma is generated in a separate chamber from that which houses the sample. These reactors are used to slowly etch diamond or change the surface termination.

**Table 2.3:** Downstream processes

| System | Gas | Flow rate | Pressure | Chuck temp. | Plasma power | Diamond etch rate |
|--------|-----|-----------|----------|-------------|--------------|-------------------|
| YES G1000 | $SF_6$ | 20 sccm | 75 mT | N/A | 200 W | 1 nm/min |
| Matrix 105 | $O_2$ | 240 sccm | 1.2 Torr | 150°C | 500 W | 0.1 nm/min |

## 2.5 Surface chemistry characterization

The surface termination and chemistry is studied with x-ray photoelectron spectropy (XPS). XPS is a well-established technique in ultra-high vacuum that quantitatively probes the chemical composition within approximately the first 10 nm of a material surface. X-ray photons, generally from an Aluminum source, are directed onto the sample, where they excite and eject core electrons in the material. The spot size of our XPS instrument (Thermo Scientific K-alpha) ranges from 35 - 400 $\mu$m in diameter. Depending on the material and its crystal structure, the excited electron can travel a short distance, also known as the "inelastic mean-free path" ($\lambda$), before losing energy as it travels through the solid. The probability of the electron being ejected from the surface and reaching the detector falls off exponentially with distance from surface (d): $I = exp(-d/\lambda)$, where $I$ is the measured intensity [Fig. 2.4a]. This means 95% of the signal comes from the top $3\lambda$ of the surface. For diamond, $\lambda$ has been calculated to be around 2 nm,[80] meaning our XPS signal reflects the chemistry within the top 6 nm of the surface.

To probe distances less than 6 nm of the surface, the sample can also be tilted such that the electrons are detected at an angle from the surface. The intensity is $I = exp(-d/\lambda \cos\theta)$, where $\theta$ is the grazing angle [Fig. 2.4b]. This means, the more the sample stage is tilted, the shallower the probing depth. At 60°, the signal comes from primarily the top 3 nm of the surface.

The kinetic energy of the electrons is measured at the detector, and is converted to the reported binding energy. The binding energy depends on the core level the

27
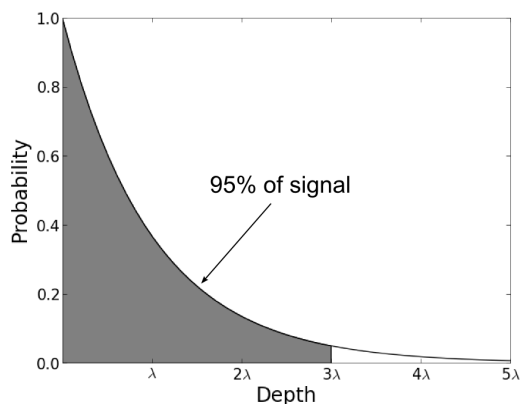
**(a)** XPS measured intensity as a function of electron depth, where $\lambda$ is the inelastic mean-free path of an electron.
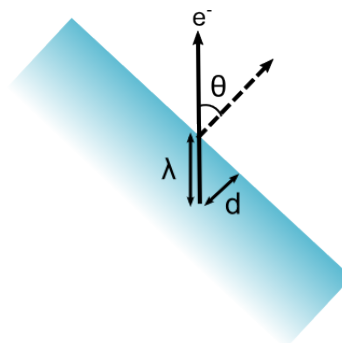
**(b)** XPS collection from a tilted sample.

**Figure 2.4**

electron originated from (s, p, d, etc) and the local chemical environment. Higher electronegative neighbors of the original atom increases the binding energy. For instance, a 2p electron pure Si will have a lower binding energy than a 2p electron from a Si bound directly to fluorine.

A common problem with XPS is charging of the substrate, which results after electrons are ejected, leaving the surface positively charged. The layer of positive charge lowers the kinetic energy of subsequently emitted electrons, and thereby changes the spectrum considerably. Since diamond is an insulating substrate, this is a particularly relevant issue. The solution is to use a flood gun of low voltage electrons to neutralize the charging effect. All XPS spectra shown in this thesis are taken with the flood gun activated.

Two types of XPS data are shown in subsequent chapters: a survey and a high resolution scan. A survey scan shows peaks corresponding to various elements, and

the integration of those peaks gives rise to the concentration of elements at the surface. A high resolution scan around one peak (e.g. C 1s) often reveals multiple peaks, which provide insight to the chemical state of the element (e.g. C-O or C-C). The fitting is done in CasaXPS, using a mixed gaussian-lorentzian lineshape for each peak.

## 2.6 Optical characterizations

All NV photoluminescence spectra were taken in a confocal set-up, either a commercially available Raman microscope (Horiba Jobin-Yvonne) or a home-built confocal set-up [Fig. 2.5]. A 532 nm continuous wave (CW) diode laser is used in both cases as an excitation source with around 1 mW power. The luminescence is collected normal from the surface with an objective with a high numerical aperture (NA = 0.9) and high magnification (100x) onto a cooled spectrometer.

In the home-built set-up (Fig 2.5), the sample sits on a piezo-controlled stage. The system is fiber-coupled, and the collected light, after being filtered through a 550 nm long pass, can be sent either to a spectrometer or to an avalanche photodiode (APD) for photon counting. Finally, the set-up is equipped with a continuous flow cryostat that cools the sample down to either 77 K with liquid Nitrogen or 4K with liquid Helium.

### 2.6.1 Optical analysis

Most of our measurements of ensemble NVs are carried out at room temperature. To gauge the health and stability of our NVs, we use the intensity of the $NV^0$ and $NV^-$ zero-phonon lines (ZPLs). We subtract away the background, because the $NV^0$ and
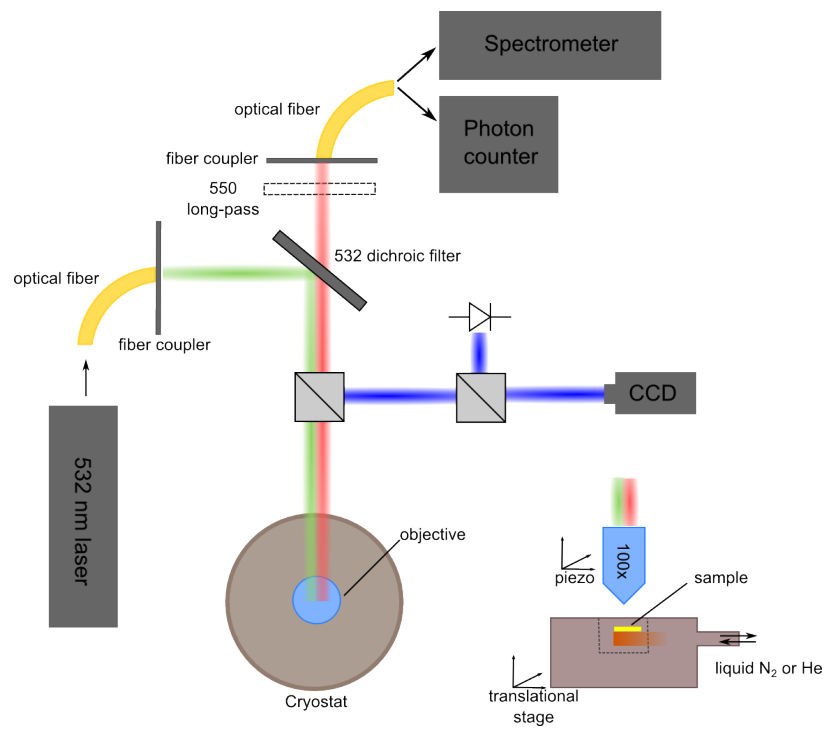
**Figure 2.5:** Home-built confocal photoluminescence set-up
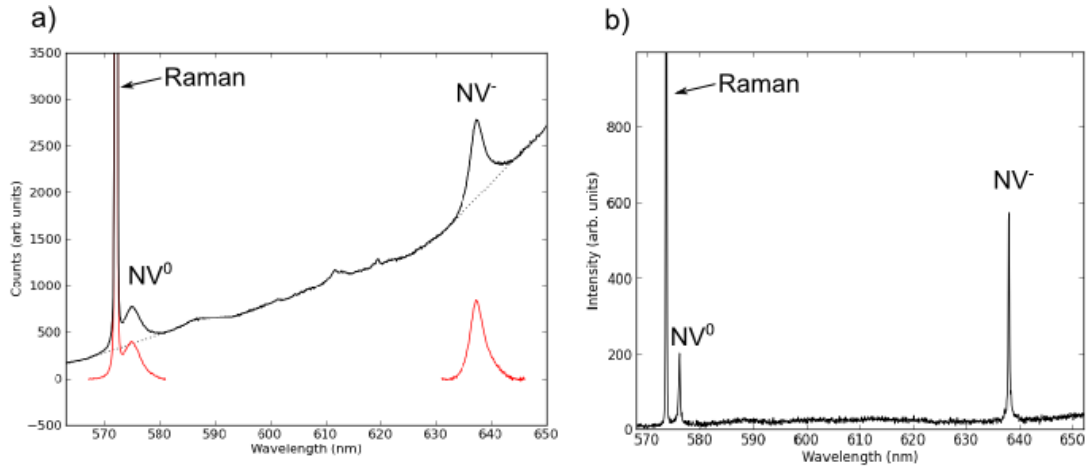
**Figure 2.6:** Analysis of NV0 and NV- ZPL at a) room temperature and b) 77 Kelvin. a) The red curves are the curves over which we integrate to find relative NV- and NV0 populations. The red curve arises from subtracting a fitted linear background (dotted line) from the original spectrum (black curve)

$NV^-$ vibrational bands overlap, which makes the absolute peak intensity an inaccurate depiction of the relative $NV^0$ and $NV^-$ populations. The resulting background-corrected peaks [Fig. 2.6a] are then integrated. At room temperature, because of the overlap between the $NV^0$ ZPL and the Raman line, only a fraction of the $NV^0$ peak is integrated. Our $NV^-/NV^0$ ratios are therefore not intended to be an absolute ratio of the charge concentration. We always use the same sample and average over many points, such that we draw conclusions only from significant changes in the $NV^-/NV^0$ ratio.

At 77 K or lower temperatures, the ZPL peaks sharpen and the background is lower due to suppressed phonon side bands. This separates the $NV^0$ peak from the Raman peak, which leads to a more accurate measurement of the $NV^-/NV^0$ ratio.

# 3

# Surface Termination

Chapter 1 introduced some of the key chemical terminations and their diamond sur-
face structures. In this chapter, we explore the effects of chemical terminations on
nearby NV emission. Near-surface NVs are notoriously unstable. Specifically, these
NVs are prone to photoblinking, where the fluorescence suddenly disappears and
reappears, and bleaching, when a prolonged exposure to laser light causes the NV
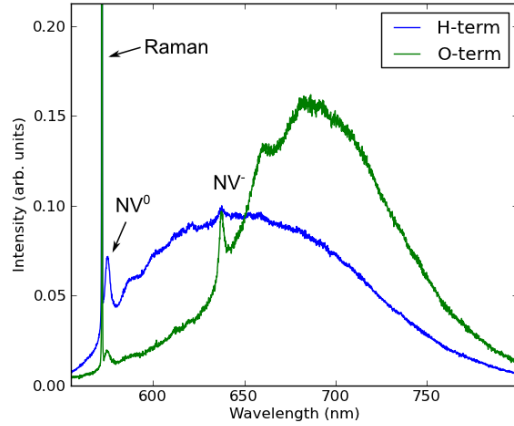
**Figure 3.1:** Photoluminescence of near-surface NV for a hydrogen-terminated and oxygen-terminated diamond surface.

fluorescence to permanently disappear. We treat surfaces with different plasmas to achieve different terminations in search of a surface that maximizes the ratio of $NV^-$ centers over $NV^0$. We also utilize x-ray photoelectron spectroscopy (XPS) to gain an understanding of the chemical composition of the surface.

## 3.1 HYDROGEN- AND OXYGEN-TERMINATED SURFACES

In section 1.3, we learned that a hydrogen-terminated surface leads to negative electron affinity and surface conductivity. As a consequence of the upward band-bending, a result of electron transfer to adsorbed water states, the Fermi level is shifted below the $NV^-$ ground state level. This results in ionizing $NV^-$ centers to its neutral charge with the top 30 nm of the surface.[63] Hence hydrogen-terminated diamonds always have a high $NV^0$ population in shallow NVs[25,20,21] [Fig. 3.1]. By applying a gate voltage across a hydrogen-terminated diamond, and the position of the Fermi

level can be shifted, and the ratio of $NV^-/NV^0$ populations can be controlled.[21] However, this method relies on having a hydrogen-terminated surface, and assumes that there are no defects on the surface that pins the Fermi level. An oxygen-terminated surface, on the other hand, result in a primarily $NV^-$ rich population, as the Fermi level generally remains above the $NV^-$ energy level [Fig. 1.3].

## 3.2    GRAPHITIZATION AT SURFACE

Hydrogen-termination is not the only way to ionize near-surface $NV^-$ centers. Graphitization, a process where $sp^3$ carbon bonds are broken and reform into $sp^2$ carbons at the surface, also acts as surface acceptor. When the concentration of $sp^2$ carbons is high, such as after a high-temperature anneal at $800°C$ in vacuum, an XPS scan of the carbon peak will be highly asymmetric and show a significant $sp^2$ C-C peak at $\approx 284$ eV [Fig. 3.2a]. The depletion of electrons near the surface results in a high population of shallow $NV^0$ centers, resulting in a PL spectrum very similar to a hydrogen-terminated surface [Fig. 3.2b]. The graphitized layer is most efficiently removed in a boiling triacid etch, which also oxygen-terminates the surface, converting the shallow NVs to mostly $NV^-$ [Fig. 3.2b].

## 3.3    FLUORINE-TERMINATION AND ITS EFFECT ON NV CHARGE

Unsurprisingly, oxygen-termination is currently the state-of-the-art surface termination for diamond. However, as discussed in chapter 1, there are many different chemical variations of oxygen-terminations, each with its own surface states and electron affinities. In particular, terminating with an alcohol group leads to a negative electron
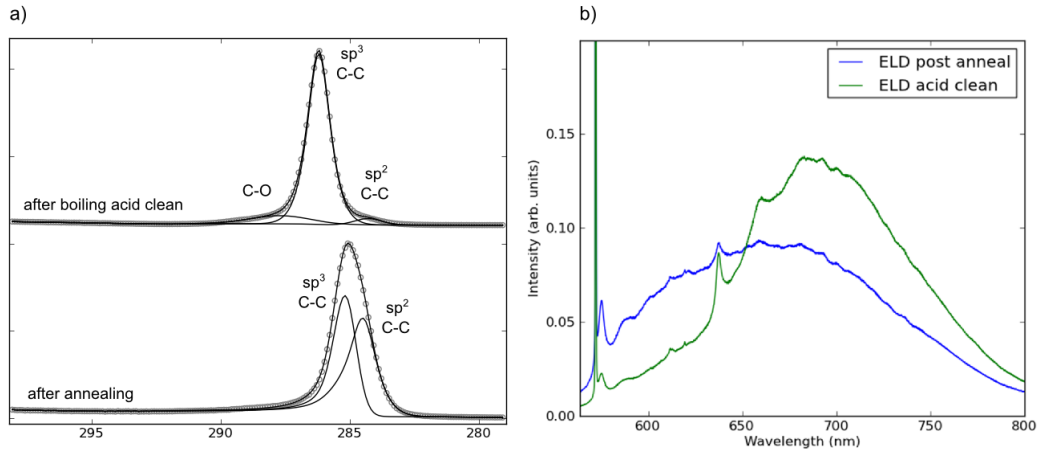
**Figure 3.2:** Surface graphitization is formed from annealing at 800°C, as seen in (a) XPS C 1s peak, and (b) its effect on near-surface NV emission.

affinity, similar to hydrogen-termination.[76,33] Furthermore, other chemical terminations to further increase the NV$^-$ population have not been thoroughly investigated.

Due to the high electronegativity of fluorine, the C-F bond is more polar than the C-O bond. *Ab initio* calculations of fluorinated diamonds show a stable and full coverage of fluorine, as well as a high electron affinity.[81] Recently, the fluorinated diamond electron affinity has been measured experimentally to be 2.56 eV, about 0.43 eV higher than for the oxygen-terminated surface.[67] Various methods have been reported in the literature for fluorine-terminating diamond surfaces, including exposure to XeF$_2$ gas,[67,19] CF$_4$ plasma,[12] and CHF$_3$ plasma.[65] In this section, we fluorine-terminate with two methods: exposure to CF$_4$ and SF$_6$ plasmas. Prior work on diamond fluorination has been confined to surface chemistry, whereas this work studies the effect of surface fluorination on the charge states of NV centers in bulk diamond.

Our studies on the effect of surface termination explore the changes on NV charge

35

ratio $[NV^-/(NV^0+NV^-)]$, which is determined through measurements of NV lumi-nescence. As discussed in chapter 2, the relative probability for the NV center to be in the $NV^-$ state is estimated by analyzing the $NV^0$ and $NV^-$ zero-phonon lines (ZPLs). Throughout the process, there was no change in overall NV intensity, only in the ratio of $NV^-$ and $NV^0$ peaks. While a small fraction of the PL signal can be attributed to intrinsic, deep sub-surface NVs, those intrinsic NVs are equally dis-tributed through the sample and any differences in the NV ratio due to the deeper NVs should accounted for in the standard deviation.

### 3.3.1 CF$_4$ PLASMA

Experiments were conducted on electronic grade, CVD-grown, (100)-oriented elec-tronic grade diamond (Element6). Diamonds were first implanted with $^{14}$N at 10 keV at $10^{12}$ ions/cm$^2$ (CORE Systems) and then annealed in vacuum at 800°C for 2 hours to create NVs approximately 15nm $\pm$ 5nm deep. Prior to fluorine-treatment, a photoresist mask (Shipley series) was deposited on half of the sample to protect the oxygen-termination. Fluorine-treatment was carried out in a Technics RF plasma reactor at 25 sccm CF$_4$ flow rate, 150 W plasma power, and 300 mTorr chamber pres-sure for 5 minutes. In all cases of plasma-treated surfaces, care was taken to avoid etching or otherwise damaging the surface by choosing plasma treatments with little or no bias voltages and minimizing the interaction time with the plasma. XPS was used to confirm that the process of depositing the photoresist mask and removing the mask with acetone and isopropanol did not affect surface chemistry.

The photoelectron spectra of the masked and CF$_4$ plasma-treated half of the same
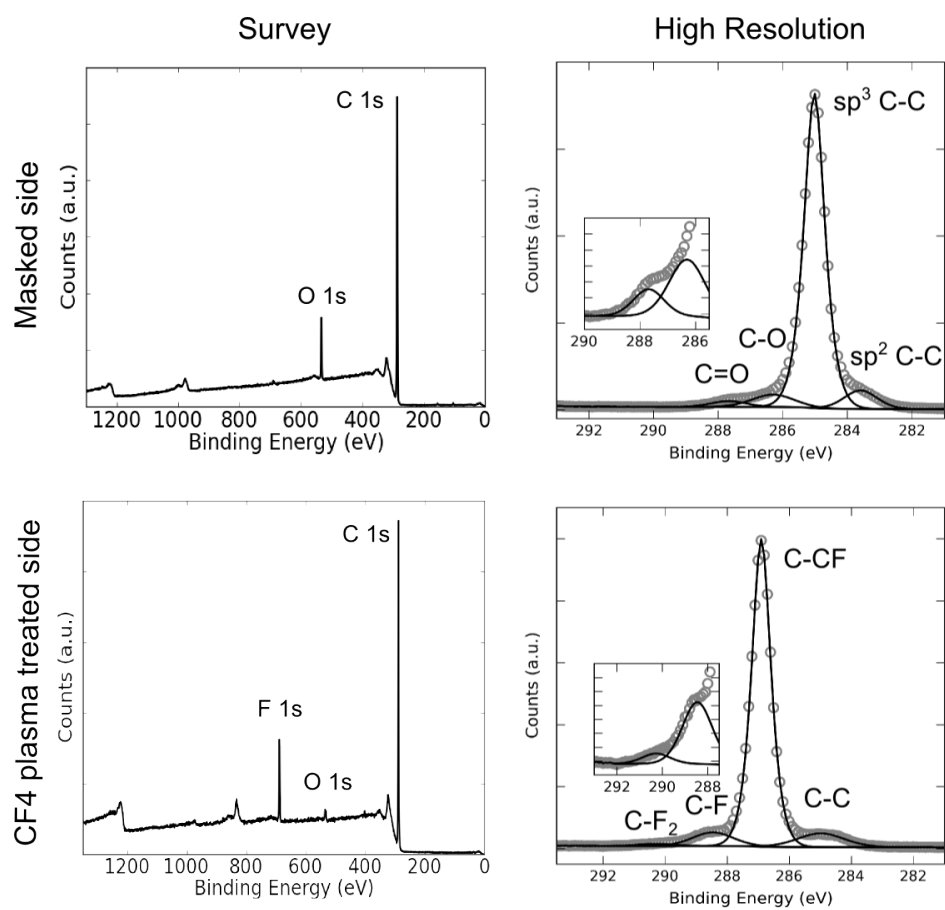
**Figure 3.3:** XPS survey and C 1s high resolution peak of the $CF_4$ plasma treated and masked surface.

sample is illustrated in Figure 3.3. The survey spectrum (left) reveals 8.5% oxygen and 91.5% carbon concentration on the masked side, whereas the side exposed to $CF_4$ shows 7.1% fluorine, 2.0% oxygen, and 90.9% carbon composition. The difference in surface chemistry between the two sides of the sample is further highlighted in the high resolution scan of the C 1s core electrons and its deconvoluted peaks. Due to the insulating nature of diamond, charging on the surface can shift the detected binding energy of electrons, even under a neutralizing electron gun. To mitigate this issue of surface charging induced peak shifts, the spectrum is calibrated by aligning the $sp^3$ C-C peak to the known literature value of 285 eV.[86] The calibration is applied to all peaks, such that the relative position of peaks are not affected. The spectrum of the masked side of the sample is calibrated by aligning the main peak to the reported value of $sp^3$ C-C bond, shifting the spectrum from the measured peak at 286 eV to 285 eV. A graphitic $sp^2$ carbon peak is visible at 283.6 eV. Two types of oxidized carbon peaks are visible at 286.3 and 287.7 eV, corresponding to C-O and C=O, respectively, evidence that the masked region is oxygen-terminated. In contrast to the oxygen-terminated side, the main peak on the unmasked side cannot be calibrated to the bulk diamond lattice, since the lowest binding energy peak is 2 eV lower than the main peak and the $sp^2$ C-C bond has only been reported to be between 0.6-1.5 eV lower than the $sp^3$ C-C.[65] The peak with lowest binding energy has been calibrated from the measured 285.4 eV to the reported 285 eV value. The main peak at 286.9 eV mostly likely reflects a C-CF bond[13,84] and the peaks at 288.5 eV and 290.3 eV (better seen in inset) correspond well to C-F and $C-F_2$ literature values.[84,1] The high concentration of C-CF bonds and the presence of $C-F_2$ suggests

some fluorocarbon deposition from the $CF_4$ plasma, which also has been reported previously in literature.[13]
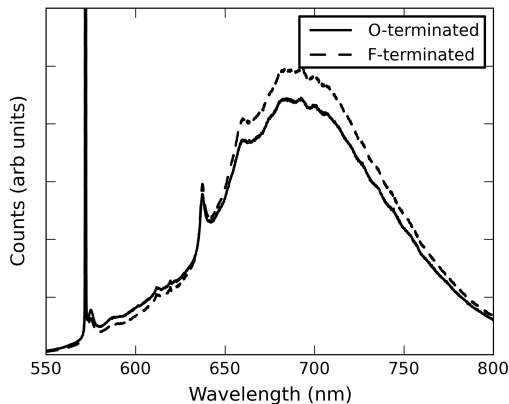


**Figure 3.4:** NV photoluminescence of oxygen- and fluorine-terminated surfaces

We tilted the stage in the XPS to vary the depth of detected electrons (see chapter 2 for the quantitative values). At higher tilt angles, as expected, the survey scan showed the fluorine signal increased in relation to carbon. In the high resolution scan of the carbon peak, we observe that the main peak shifts to higher binding energies at higher tilt angles [Fig. 3.5]. We believe this due to a polymerized fluorocarbon layer at the surface, and the primary carbon component is bound to an increasingly larger number of fluorines. At 60 degree stage tilt, the highest intensity peak is pure C-F, and the smaller side peaks with higher binding energies correspond to $C-F_2$ and $C-F_3$. Since at 60 degrees we are probing the top 3 nm of the surface, and the $sp^3$ C-C peak has completely disappeared, we estimate the polymerized fluorocarbon layer to be about 3 nm thick.

To measure the effect of surface termination on NV emission, we measured the PL
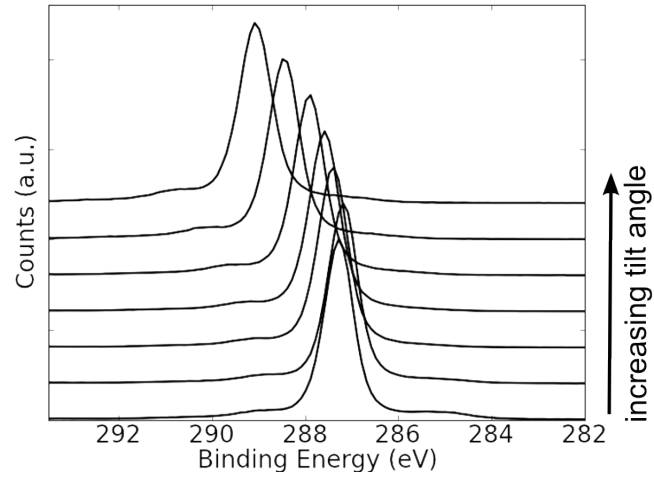
**Figure 3.5:** High resolution C 1s XPS taken of a $CF_4$ plasma treated sample at tilt angles from 0 to 60 degrees.

a)

b)
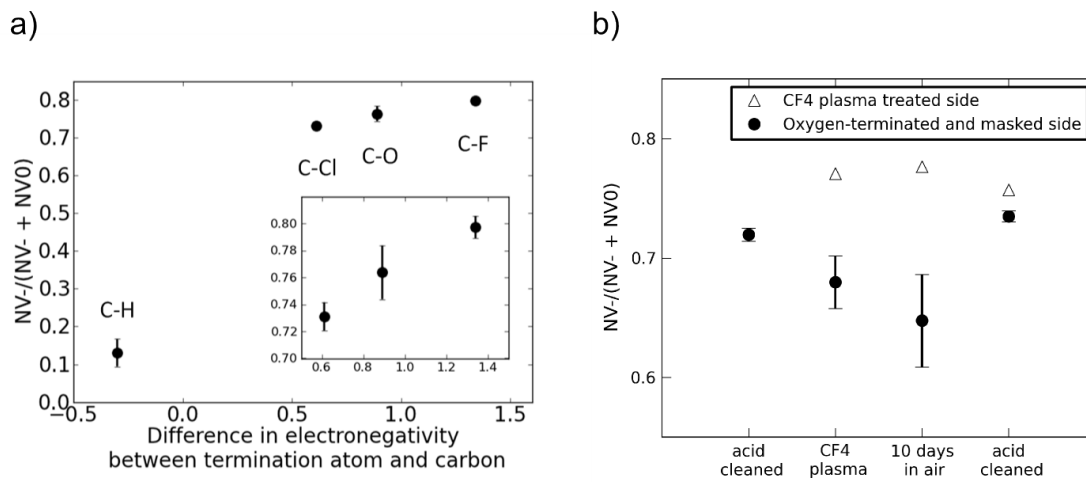


**Figure 3.6:** (a) $NV^-$ ratio for various surface terminations. (b) $NV^-$ ratio stability over time

before and after treatments [Fig. 3.4]. We started with a boiling triacid-cleaned and oxygen-terminated surface, where PL was taken at multiple points over the whole sample. PL of an oxygen-terminated sample is shown in Figure 3.4. Error bars here represent standard deviations in the calculated ratio between three to nine spots on the sample. After masking and treating with $CF_4$ plasma, a relative increase of $NV^-$ was observed on the fluorine-terminated side [Fig. 3.6]. The fluorine-terminated side remained stable after exposure to air for ten days, whereas the $NV^-$ ratio on the oxygen-terminated side was further degraded. The lack of stability of the oxygen-terminated surface is not fully understood and further investigation is required. However, we do note that oxygen-termination is a mixed chemical state on the surface and can exist as hydroxyl groups, ethers, ketones, or carboxylic acids. Consequently, the oxidation state and the oxygen coverage can change upon reaction with moisture in air, which changes the surface energy, thereby destabilizing nearby NVs. The thin polymerized fluorocarbon layer on the $CF_4$ treated side, however, can protect the surface against oxidation and other surface degradations. Contact angle measurements also show that the fluorinated surface is more hydrophobic than the oxygenated surface [Fig. 3.7]. We were able to return the whole sample to its oxygen-terminated state by first annealing at 300°C in air to remove the fluorocarbon layer, then treating with boiling triacid. The $NV^-$ / ($NV^0$ + $NV^-$) ratio on both sides of the sample converged to approximately the initial value [Fig.3.6].

We compared the effect of hydrogen-, oxygen-, and fluorine-termination without a photoresist mask with a different diamond sample, implanted with $^{14}N$ under the same conditions. The sample was first hydrogen-terminated in a $H_2$ plasma by flowing
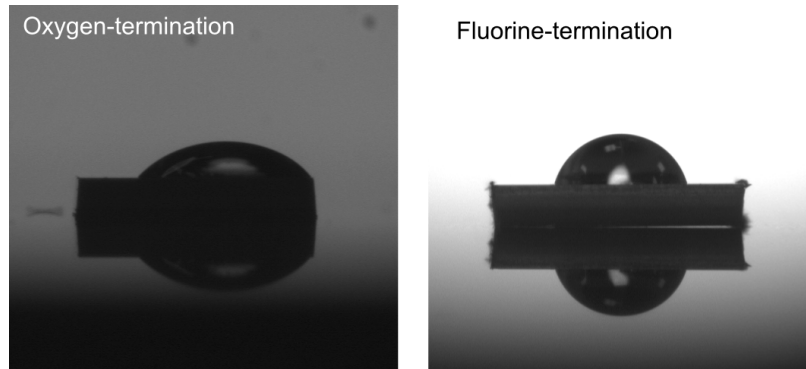
**Figure 3.7:** Contact angle of water on oxygen- and fluorine-terminated surfaces

400 sccm of $H_2$ in a CVD reactor at 60 torr pressure with a 700 W plasma power for 3 minutes. Next, oxygen-termination was achieved with the boiling triacid clean, and finally the sample was fluorine-terminated with $CF_4$ plasma. Between each step, we measured PL at several spots and compared the $NV^-$ and $NV^0$ signals. Our experimental results indicate more electronegative terminations lead to higher relative $NV^-$ concentration [Fig. 3.6]. Fluorine-termination could induce a downward band-bending,[67] and the strength of the surface dipole can play a significant role in electron density at the surface, thus increasing the relative $NV^-$ signal. Additionally, it is important for the surface termination to have good coverage, since dangling bonds can be electron traps. Previous theoretical calculations show fluorine adsorption energy remains low for all coverages, meaning it is possible to have a full monolayer of F on a diamond (100) surface, whereas full and stable coverage is less likely for other terminations, such as Cl.[81] While this is theoretically possible, we do not know the degree of coverage of fluorine in our samples.

### 3.3.2 $SF_6$ PLASMA

It is unclear if the NV stability and increased NV$^-$ signal is due to the fluorocarbon layer or the fluorine-termination at the surface. To avoid the formation of a polymer, we treated the surface with $SF_6$ plasma instead of $CF_4$. We used a diamond, again with implanted ensemble NVs $\approx$ 15 nm deep. Half of the sample was masked with photoresist before exposing the diamond to a $SF_6$ plasma downstream for 2 min. Detailed conditions for the process are found in Table 2.3.

After the $SF_6$ plasma treatment, we first analyzed the surface chemistry with XPS [Fig. 3.8]. A survey scan found the surface was comprised of 87% carbon, 4% oxygen, and 9% fluorine, a higher concentration of oxygen than the $CF_4$ plasma treated sample. A high resolution scan of the C 1s peak confirmed that there was a greater percentage of C-O bonds than was true for the $CF_4$ plasma treated surface [Fig. 3.8b]. However, covalent carbon-fluorine binding is also evident from the C-F$_x$ peaks around 290 eV. When the sample was tilted, no shift was seen in the main peak [Fig. 3.8b]. The only consequence of probing a more shallow region of the surface was higher ratios of C-F, C-O, and sp$^2$ C-C. This indicates that all those species are bound to the surface, and that the diamond sp$^3$ C-C lattice makes up the majority of the carbon signal.

Next, photoluminescence measurements in our home-built set-up [fig 2.5] were used to elucidate any changes in the NV charge ratio. As mentioned in section 2.6.1, photoluminescence taken at 77 K results in sharper ZPLs and a lower background due to suppressed vibrational bands. In particular, the NV$^0$ peak is more easily distinguished from the Raman line (c.f. Fig. 3.4 and Fig. 3.9a), which gives a more
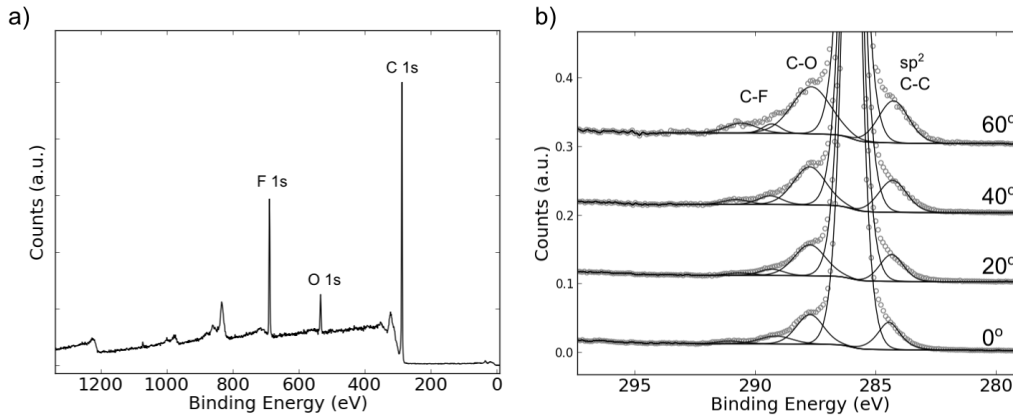
**Figure 3.8:** XPS of sample exposed to SF$_6$ plasma downstream. (a) Survey scan, showing 87% carbon, 4% oxygen, and 9% fluorine. (b) High resolution carbon XPS taken of a SF$_6$ at sample tilt angles from 0 to 60 degrees.

accurate estimate of the NV ratio. After the sample was cooled to 77 K, measurements were made at eight points over a 1×1 mm area of the masked and SF$_6$ treated sides. The NV$^-$ ratio [Fig. 3.9b] is calculated from the photon counts at the ZPL peaks, and the standard deviation represents the variation over the eight points. We found no difference in the NV charge ratio between the oxygen- and fluorine-terminated sides of the sample. Next, we cleaned the sample with boiling triacid to oxygen-terminate both sides of the sample again. The NV$^-$ ratio seemed to decrease, but this could be due to errors in the PL set-up. The spectra were taken a week apart from each other, and small changes in the optical set-up resulted in PL signals an order of magnitude dimmer than was true for the original spectra.

To decrease the oxygen concentration at the surface, we tried other ways of fluorine-termination. Samples were exposed to XeF$_2$ gas, a gas which decomposes readily when in contact with water vapor and is used to etch silicon. Unfortunately, XPS did not show any covalent bonds between the diamond and fluorine after the

**(a)** NV photoluminescence at 77K after $SF_6$ treatment

**(b)** $NV^-$ ratio for fluorine-terminated surface through $SF_6$ treatment
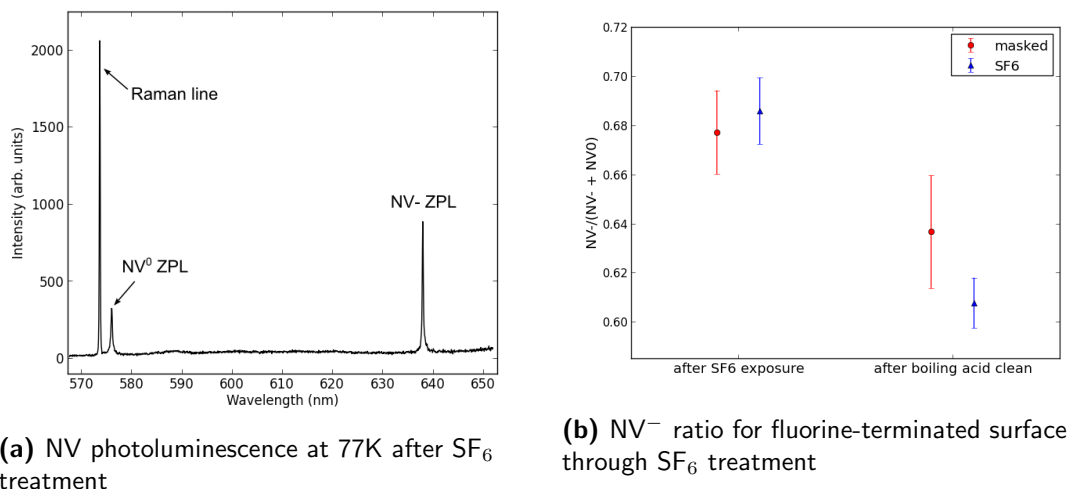
**Figure 3.9**

sample was rinsed in solvent. Other non-silicon reactions with $XeF_2$ required elevated temperatures. We did successfully fluorine-terminate the diamond with $SF_6$ plasma in an isotropic etcher (process conditions in Table 2.2). However, XPS revealed a surface very similar to that produced by the downstream etcher, also with high oxygen concentrations. Preliminary room temperature measurements indicated no improvements in $NV^-$ ratio through this process. Higher fluorine coverage was achieved with $SF_6$ plasma in an inductively-couple reactive ion etcher. XPS survey scans showed only 1% oxygen, similar to the $CF_4$ plasma treated sample. However, as will be discussed in chapter 4, this process, despite a minimal etching removal of the diamond, led to significantly dimmer NV emission. We believe this to be evidence of damage of the $SF_6$ on the nearby NVs.

It is still possible that the higher dipole moment at the surface due to C-F bonds increases the concentration of $NV^-$, but the difference is masked by the high con-

centration of C-O bonds at the surface. It seems a mix of oxygen- and fluorine-termination does not result in any discernible effects on NV charge states. More work needs to be done to better fluorinate the surface. From the current preliminary data we have on $SF_6$ treated surfaces, we believe the NV stabilization and the increase in NV charge state seen on the $CF_4$ plasma treated surfaces was due to the fluorocarbon polymer at the surface.

### 3.3.3 Fluorine-termination on other NV properties

We were interested to see if fluorine-termination affected any other NV properties besides the charge ratio. We used a sample also implanted at 10 keV but with a lower density of $10^{10}$ ions/cm$^2$. At this density, we expected to observe some isolated, single NVs. As before, we masked the sample with photoresist, and exposed the sample to 1 min of $CF_4$ plasma. We then removed the photoresist to expose a half oxygen-terminated and half fluorine-terminated surface.

First, we looked to see if the ZPL linewidth was affected by the surface fluorination. Linewidth broadening can be due to spectral diffusion, a sign of charge switching in NVs. Our collaborators, L. Bassett at UCSB, measured the $NV^-$ ZPL linewidth with on-resonance excitation of 637 nm at 4K, identifying 10 individual NVs on the oxygen-terminated side and 8 on the fluorine-terminated side. The linewidths measured of these implanted, near-surface were in the 10s of GHz, expected for near-surface implanted NVs. Unfortunately, there was a large deviation of measured linewidths throughout the sample. No difference between the linewidths of the oxygen- and fluorine-terminated sides were observed within the variations of linewidths measured.

Next, we compared the $T_2$ spin decoherence lifetime between the two sides of the same sample. Near-surface NV spin lifetime is often shortened by a bath of surface electron spins, and we were interested the effect of the deposited polymer. Our collaborators in D. Rugar's group at IBM measured the $T_2$ lifetime, and also found a large variation, ranging from a few microseconds to 100s of microseconds. We believe the deviation was again due to the straggle in NV depths. The spread in $T_2$ lifetimes made elucidating any effect on the NVs difficult. There has been another report, noting no difference in the $T_2$ lifetime between oxygen- and fluorine-termination on NVs in a 5 nm thin layer diamond film.[57]

Since our initial publication, two other groups have also reported an increase in NV$^-$ signal following $CF_4$ treatment.[57,59] Ohashi reported that 30% of the 2-5 nm deep NVs measured on the fluorine-terminated sample bleached out after extended exposure to laser illumination.[57] Such bleaching was not evident in either oxygen- or hydrogen-terminated surfaces. This could be explained by a model that found localized acceptor states close to the conduction band in fully fluorinated diamonds.[33] On the contrary, Osterkamp reported that $CF_4$ plasma caused the 3 nm deep NVs to stop blinking.[59] The discrepancy between reported results so far could be due to differences in the fluorine-coverage at the surface and the details of their fluorination process.

## 3.4 SUMMARY

There are two well-known and characterized surface acceptors: adsorbed water layers on a hydrogen-terminated surface and $sp^2$ carbons. These acceptors result in surface

band bending and ionize nearby NVs to its neutral charge. To combat this, oxygen termination is used to induce a higher concentration of $NV^-$ centers. Consequently, oxygen termination is considered as an ideal surface. However, we have shown here that prolonged contact to air could result in a decrease in $NV^-$ population. A key issue with oxygen termination is the various possible chemical bonds between carbon and oxygen. Future work could involve an in-depth study of the relative concentration of different oxidation states. It would be particularly insightful to understand how the oxygen coverage and chemical states vary when oxygen-termination achieved through acid clean, oxygen plasma, and low temperature anneal in oxygen gas.

A fluorine-terminated surface was proposed and shown to lead to higher concentrations of $NV^-$ centers. The highest concentration of fluorine at the surface has resulted from a short exposure to $CF_4$ plasma, which forms a polymeric fluorocarbon layer at the surface that protects nearby NVs. No significant changes in the NV linewidth or spin decoherence have been seen yet, likely due to the large scatter in their values.

To better understand how near-surface NVs are affected by fluorine-termination, we want to ideally follow single NVs at a uniform distance from the surface. Furthermore, a higher coverage of fluorine, without the formation of fluorocarbon polymer, would allow us to better understand the effect from only the fluorinated modification of the surface. This could be achieved by exposing a heated or otherwise activated diamond surface to $XeF_2$ gas.

Stabilizing near-surface NVs is one of the biggest obstacles in current NV applications. Our results here raise questions about the existing state-of-the-art surface.

Furthermore, the demonstrated plasma treatments may become a relevant tool for depositing films on the diamond surface for spin-coupling.

# 4

# Plasma induced damage

Diamond is a hard and inert material, and can only be shaped through dry etching. Most commonly, diamond is etched in an inductively-coupled reactive ion etcher, which involves high energy ions physically sputtering away diamond. From studies in other materials, such as Si and GaAs, we know sub-surface damage occurs during these processes. Characterization and minimizing the damage caused by dry etching

is an important part of diamond device fabrication for all applications. In particular, we want a reliable way of bringing NVs to <2 nm from the surface for better sensing of external spins. At those depths, NV creation, whether through CVD incorporation or ion implantation, have very low conversion efficiencies,[64,58] which results in an excess of unnecessary defects. Thus, we want to start with NVs a bit deeper from the surface, and then bring them closer to the surface through a measured, reliable, and non-damaging method. However, a primary obstacle of near-surface NVs is their sensitivity, and that they can be easily dimmed or annihilated through damaging processes such as plasma etching.

Previously, the only method proposed for short etches in diamond that minimizes damage is through slow oxidative etching by annealing to 600°C in air.[44] While this method is very promising, an exact etch rate is very difficult to extract. The etch rate varies greatly depending on small changes in the temperature. The position of the diamond in a tube furnace set at the same temperature can result in a drastically different etch rate. Moreover, masking and patterning the sample is unfeasible. Dry etching is thus still the preferred method for removing diamond.

In this chapter, we study NV emission and diamond surface chemistry to characterize plasma damage. We explore the effect of different gases ($H_2$, $O_2$, $Cl_2$, $SF_6$) and etch systems on NV luminescence. We also explore inherent the effect of bringing an NV closer to the surface.

## 4.1 Brief introduction to plasma etching

### 4.1.1 Plasma reactors

Reactive ion etchers can be classified in various ways. In this work, we will be primarily considering three kinds of etchers: reactive ion etcher (RIE), barrel reactor, and downstream etcher [Fig. 4.1].

**Reactive ion etcher**  **Barrel reactor**  **Downstream etcher**
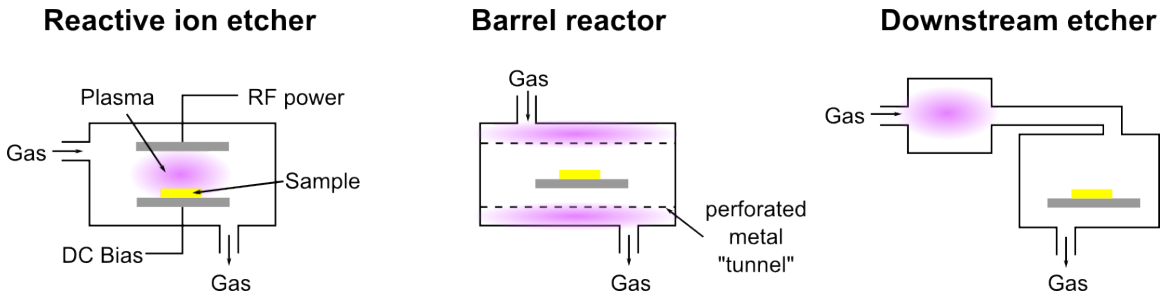
**Figure 4.1:** Three types of dry etching systems

In all plasma etching systems, a chemically active plasma needs to first be generated, usually by applying a strong time-varying radio frequency (RF) electromagnetic field at 13.56 MHz to a chamber of gas molecules. In an inductively coupled plasma reactive ion etcher (ICP RIE), this energy is delivered inductively through a coil wrapped around the chamber. The RF field strips the gas molecules of their electrons, creating high energy ions and radicals. These reactive species attack and react with the surface of the material, creating stable compounds that leave the surface and get pumped away. In a typical RIE system, there is a natural or enhanced large voltage difference between the plasma and the grounded wafer, which accelerates the charged ions towards the surface. The increase in kinetic energy, which results in physical sputtering of the material in addition to the chemical reaction, leads to

anisotropic etches with straight side walls.

In the barrel reactor, the plasma is generated around the wafer, and the reactive species diffuse in through the perforated metal. The barrel reactor therefore has no DC bias. It is a less damaging method, and is generally used for stripping resist, where the isotropic nature and slow etch rates are not an issue. Even in a barrel reactor, however, highly sensitive devices can suffer. There is UV radiation from the generated plasma, which break chemical bonds and have been known to cause damage in semiconductor fabrication.[31] Furthermore, since the ions and radicals are still highly energetic, physical sputtering still accounts for some of the etching.

One of the gentlest ways of etching is in a downstream mode, where the plasma is formed in a separate chamber from the wafer. The most reactive and energetic ions and radicals collide with the walls. By the time the ions reach the wafer, no physical bombardment occurs, only slow, isotropic, chemical etching is observed. In such a system, the wafer is often heated to speed up the chemical reaction at the surface. In all systems, there are several additional important factors that can greatly affect etch conditions, including plasma density, RF power, and chamber pressure.

### 4.1.2   PLASMA DAMAGE

Plasma damage has been mostly studied in common semiconductor materials, such as Si and GaAs. The damage reported comes primarily from the flux of high energy ions bombarding the surface. In RIE, the projected range of ion implantation in the substrate depends strongly on the bias voltage, and generally extends no more than 2 nm. Ion diffusion however can result in modifications to the material 50 nm from

the surface.[55]

One relevant study observed luminescence of GaAs quantum wells (QWs) 30, 60, 90, and 446 nm from the surface as a function of etch times and bias voltages.[85] After etching in Ar with 500 V bias, they found the cathodoluminescence (CL) of QWs dimmed significantly. The majority of the damage occurred within the first 60 nm of the surface, but damage was propagated past 90 nm, which can be attributed to ion channeling. A lower bias voltage (350 V) resulted in less dimming of QW CL, and is thus considered less damaging. It was also found that a long sputtering time does not result in damage penetrating any deeper into the sample, but the damage became more pronounced. They suggested that reactive ion etching creates non-radiative deep-level defects.

Plasma damage in diamond and their effect on NVs has not been extensively studied. A recent study showed that a 20 second exposure to $O_2$ in ICP RIE (calibrated to etch remove 10 nm of diamond) resulted in the complete disappearance of NVs 20 nm deep.[35] After 2 hours of vacuum anneal at 800°C, they generated new NVs with a higher density than before. They proposed that the short etch generated additional vacancies at shallow depths, which upon annealing, formed new NV centers with other interstitial NVs created from implantation.

Nitrogen-vacancy centers, especially near the surface, are known to be extremely sensitive to the environment. Therefore, they act as a great test-bed for plasma damage. Many of our experiments involved very slowly etching diamond and measuring the effect on nearby NVs.

## 4.2 Damage from H$_2$ plasma etching

We first tested the result of hydrogen plasma etching on our near surface NVs because it has been found to help smooth the (100) surface and remove graphitic phases.[32] Our process gave us etch rate of 1 nm / min, which is slow enough to methodically bring NVs closer to the surface. We minimized the damage by maintaining the bias power below 100 V and by cooling the back side of the sample in the reaction (see profess #1 in table 2.1 for additional details).

We used a sample with ensemble NVs delta-doped $50 \pm 20$ nm from the surface, and protected regions of it by masking with photoresist. To our surprise, after etching about 1 nm of diamond from the surface, the NV signal completely disappeared [Fig. 4.2]. We oxygen-terminated the sample in a barrel reactor with O$_2$ plasma and still found no NVs. Regions masked by the photoresist showed no change in NV luminescence. Annealing the sample in O$_2$ up to 465° for a few hours also did not revive the photoluminescence signal.

It is known in literature that due to its small size, hydrogen atoms diffuse easily and deeply through the lattice.[55] Doped silicon has been shown to lose its conductivity due to hydrogen passivation of acceptors.[55] In diamond, the diffusion constant was estimated to be $(0.6 \pm 0.3) \times 10^{-8}$ cm$^2$/s.[77] Reduced fluorescence was seen for NVs greater than $80\mu$m deep after 8 min exposure of 1.5kW hydrogen plasma at $>700°$C. The group was also unable to recover NV emission through oxygen treatments or annealing up to 1100°C. It is believed that the diffused hydrogen can be trapped by NVs to form NVH centers, and other groups have reported the NVH complex is stable
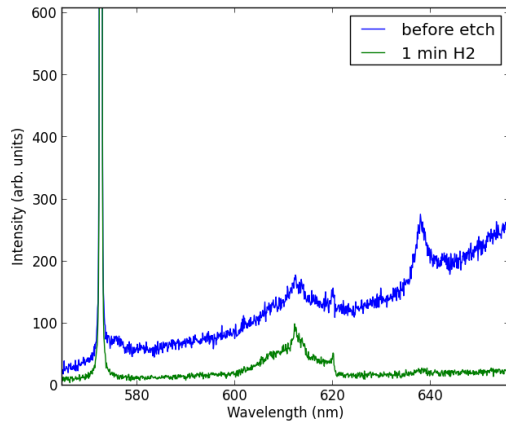
**Figure 4.2:** Photoluminescence of the NVs before and after 1 min etch in 600 W of $H_2$ plasma. The peaks at 573 nm and between 600 - 620 nm are primary and secondary diamond Raman peaks, respectively.

against annealing up to 1600°C.[34]

We have shown that NVs are irreparably damaged despite being exposed to milder conditions than previous reported and after only 1 nm of etching. Hydrogen plasma etching is thus not recommended for near-surface NVs.

## 4.3   O2 PLASMA DAMAGE: SINGLE NV STUDY

Oxygen is the most commonly used gas for diamond fabrication. Etching in oxygen plasma, like hydrogen, relies partially on chemical reactivity, which results in higher etch rates. In addition, the resulting surface is oxygen-terminated, which is favorable for NVs. For these reasons, oxygen plasma is considered to be least damaging.

To test for damage caused by oxygen plasma, we counted the number of single NVs before and after exposing to oxygen plasma in a barrel reactor. The optical measurements were taken by A. Greenspon. We used a sample that was implanted

with nitrogen at 10 keV at $10^{10}$ ions/cm$^2$ density, yielding us mostly single NVs, which was confirmed with antibunching measurements. A scan with an avalance diode photodetector (APD) [Fig. 4.3a] shows isolated NVs.
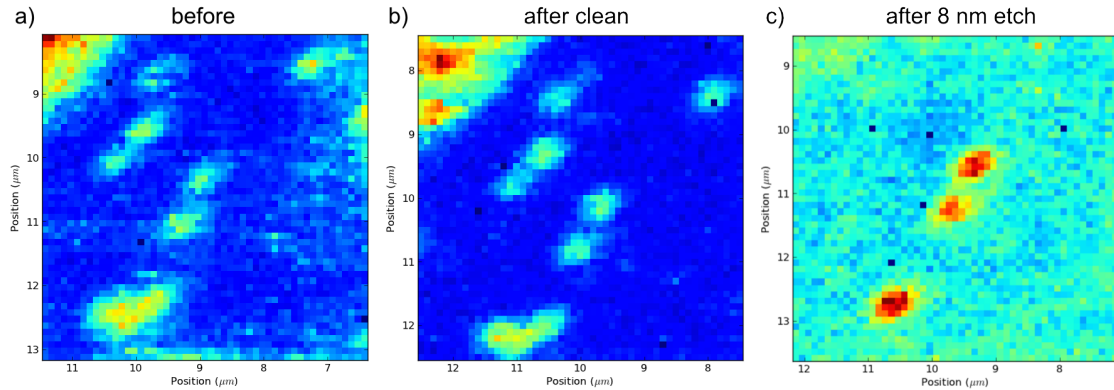


**Figure 4.3:** Counts of photoluminescence of the same 5 × 5 $\mu$m region before, after boiling triacid clean followed by oxygen anneal at 465°C, and after an etch. Scan images courtesy of A. Greenspon.

We etched a few markers into our sample to ensure we can compare the same regions before and after the etch. This process was carried out by A. Greenspon. We used a direct write lithography system (Heidelberg Instruments) to pattern a grid of triangular openings (2 × 3 $\mu$m), 15 × 15 $\mu$m apart. The mask material was SiO$_2$. We then etched the triangle shapes approximately 30 nm deep, such that the pattern was visible under the microscope. We chose this method of permanently marking our sample instead of depositing a mask, such that the markers would not be removed during our processing.

We took 35 5 × 5 $\mu$m APD scans to get a statistical count of NVs. Next we cleaned the sample in boiling triacid and annealed it at 465°C. Comparing a photon count scan of the same areas 5 × 5 $\mu$m area before and after the clean [Fig. 4.3a and b], we did not see any change in NV density in our APD scans [Fig. 4.3b]. This

was consistent with our ensemble NV measurements, where we do not see a higher counts in the NV ZPL. We noticed that the background had brighter regions before the clean, likely due to organic contamination on the surface that fluoresces or due to particles backscattering the incident laser light.

Next we etched the diamond in a barrel reactor for 10 min (see table 2.2 for details), which results in a 8 - 10 nm etch depth. After going back to the same regions and scanning the areas again, we found that only 25% of the total NVs survived. In figure 4.3c, for instance, we can see that only 3 out of 8 of the NVs remain. Some scan regions had no surviving NVs. We also noted that the background count level was higher, likely because the surface roughened in the process. As discussed later, etching in the barrel reactor leads to slightly higher surface roughness, which result in more backscattering in the incident laser.

As discussed in section 2.1.1, some straggle in the z direction is expected with the ion implanted NV samples, which means etching up to 10 nm of diamond results in the removal of some NVs. However, as the simulation of the nitrogen distribution at 10 keV implantation energy shows [figure 2.2], it is not possible for 75% of ions to be within the first 10 nm of the sample. We therefore conclude that the plasma etch process is damaging the lattice and quenching near-surface NVs in a irreparable manner.

## 4.4 O2 plasma damage: ensemble NV study

To better characterize the damage, we need to use a delta-doped sample, where the NV distance from the surface has a much smaller distribution. It is also important to

measure the actual distance to the surface, which is most accurately achieved through sensing of electron spins or protons at the surface.

In these series of experiments, we compared the effect of slowly etching the diamond with oxygen plasma in an ICP RIE, a bench-top photoresist stripper. NV luminescence was monitored at each step to gauge its health. Finally, we extracted the actual depth of the NV with spin measurements.

### 4.4.1 EXPERIMENTAL PROCESS

An electronic grade diamond with ensemble delta-doped NVs $\approx 50$ nm $\pm$ 20 nm from the surface was used. The large range in potential NV depth is due to fluctuations of the diamond growth rates.[58] The process for estimating the exact starting NV depth will be discussed later. Most importantly, however, given some depth, z, the straggle of the NV position ($\Delta$z) is confined to $\pm$ 4 nm.
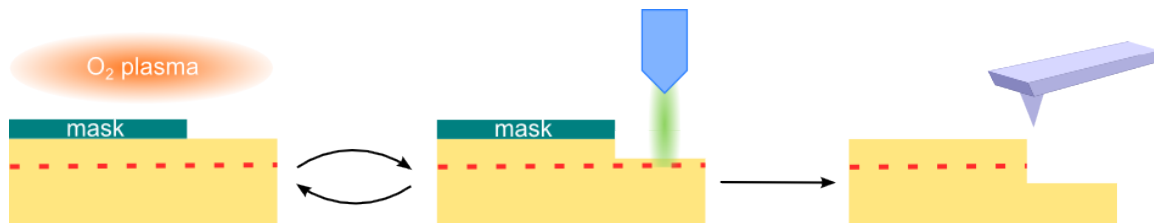


**Figure 4.4:** Experimental procedures for sequential oxygen-plasma etching

A schematic of the experimental process is shown in figure 4.4. First we mask the majority of the sample with silicon dioxide to protect it from any damage, as described in chapter 2. Then we sequentially etch the sample with oxygen plasma. After each step of etching, the NVs are characterized in a commercial set-up (see chapter 2 for more details). We then measure the NV photoluminescence at several

points over the same region (around $300 \times 100$ um area of the sample), using the same acquisition parameters. Figure 4.5 shows a map of the $NV^-$ luminescence in the same region of the sample after incremental etch times. Each step, consisting of an etch and photoluminescence measurement, is repeated until no more NV emission is seen. The mask is then removed, and the final step height is measured with an AFM.
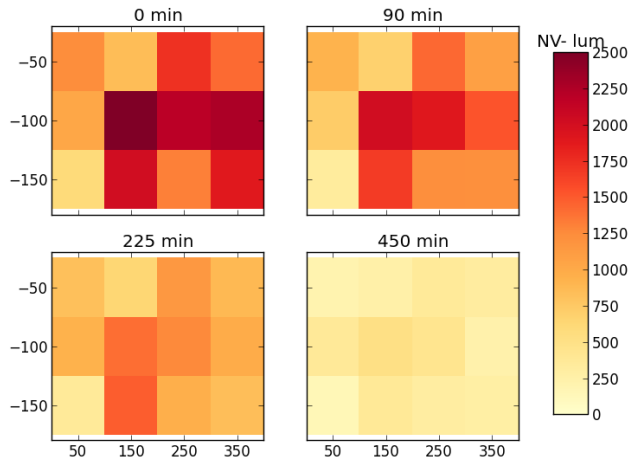


**Figure 4.5:** PL map of the same region after incremental time etched in a downstream etcher. Z axis shows the luminescence intensity at 638 nm, corresponding to the $NV^-$ ZPL.

The same sample underwent this sequential oxygen etch in three different reactors: an ICP RIE reactor (Unaxis), a bench-top resist stripper (Technics), and a downstream system (Matrix).

Each etch step in the ICP RIE was 30 seconds of a low bias $O_2$ plasma (see Process #3 in 2.1 for process conditions). We optimized the process condition to achieve the minimal bias (50 V) while still sustaining a stable plasma. This not only minimizes damage caused to the material, but also limits the etch rate. The transfer chuck on

which the sample sits is cooled in the system to room temperature.

The bench-top resist stripper, hereon out referred to as the Technics, is closest to a barrel reactor. The $O_2$ plasma is generated isotropically around the sample, which sits on a grounded tray. No external bias is applied to accelerate the ions from the plasma. One etch step in this reactor was set at 10 min of etching [see table 2.2 for process conditions]. The instrument has no cooling mechanism, so the plasma is only lit for 5 min at a time, before the sample is taken out to cool back down to room temperature. We estimate the temperature to rise to about 60-80°C after 5 minutes.

In the downstream system, the plasma is generated in a quartz chamber above a second chamber, which houses the sample. A quartz baffle blocks the line of sight between the chuck and the plasma. We attach the diamond sample to a silicon carrier wafer with thermal paste. The wafer is then transfered into the reaction chamber where it rests on a hot plate heated to 150°C. Each etch step in the downstream reactor, using the conditions from table 2.3, was set at 45 min.

### 4.4.2  ETCH RATE AND SURFACE ROUGHNESS

To estimate the total etched depth after the sequential etching was done, we removed the $SiO_2$ mask with HF and used an AFM to measure the height of the step edge [Fig. 4.6b]. In the ICP RIE sample, we found that a 30 second etch resulted in 8 nm of removed diamond, meaning $4 \times 30$ sec steps resulted in a total etched depth of 32 nm. The measured step height of our sample after 40 min of etching in the Technics was 50 nm. The total step height of the sample, after 510 min of etching in the downstream reactor, was 55 nm. Assuming a constant etch rate, each etch step

in the Technics and downstream etcher corresponds, respectively, to 12.5 and 4.8 nm of diamond removed.
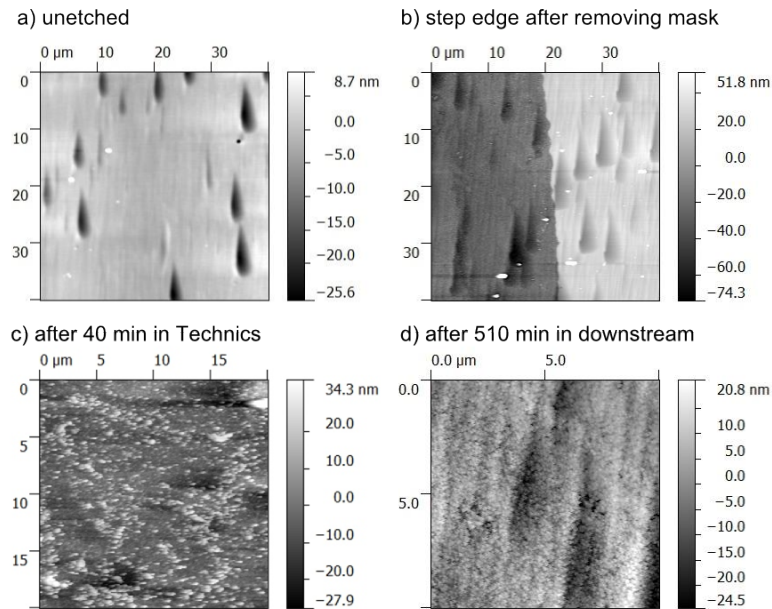


**Figure 4.6:** AFM of delta-doped sample. The scan area of the surface after the downstream etch is smaller to show the surface roughness better

The etched region became significantly rougher after 40 min of Technics and 8.5 hours of downstream etching [Fig. 4.6c and d]. The RMS roughness in the unetched region [Fig. 4.6a] increased from 2 nm to 10 and 7 nm after etching in the Technics and downstream, respectively. The sparsity of the roughness in Technics leads us to believe that micromasking, the redeposition of the mask material onto the etched surface, was at play. The higher density of roughness after such long downstream etch does not come as a surprise, since downstream etching relies entirely on isotropic, chemical etching. Therefore, after 50 nm of etching, the surface was only getting rougher, and not etching down uniformly. Because of this, downstream etching is not
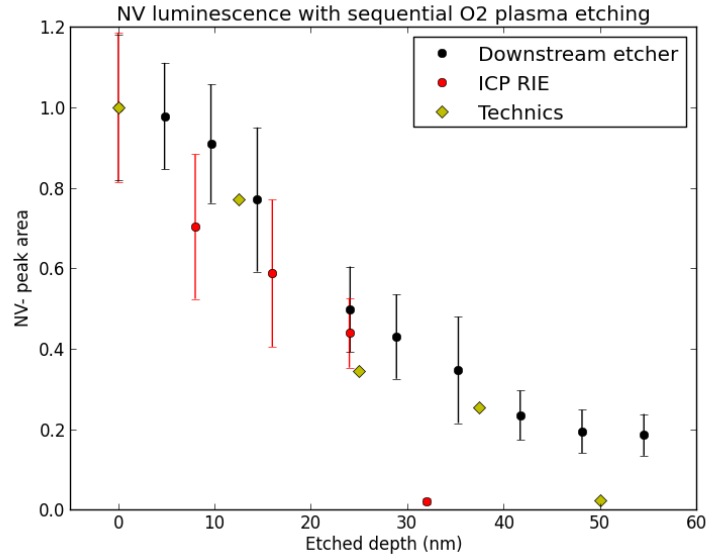
**Figure 4.7:** NV$^-$ photoluminescence signal after etching in either an downstream or ICP RIE system.

designed to etch such large amounts of material. In contrast, the ICP RIE process does not roughen the surface until after 5 min of etching.

### 4.4.3  RESULT: NV LUMINESCENCE AND NV DEPTH

Equipped with an estimate of the etched depth at each step, we can compare the relative change in NV luminescence between etching in the ICP RIE, Technics, and downstream etcher. The NV$^-$ intensity at various etched depths for each instrument is shown in figure 4.7. The plotted NV$^-$ signal is the integrated NV$^-$ peak as discussed in section 2.6.1, normalized by the initial NV signal before any etching occurred. Each point represents the average and standard deviation of NV signal measured at multiple locations in the sample, as seen in figure 4.5. The error bars in the Technics data have been removed from the figure for clarity, but are similar in size.

There are two results of interest from figure 4.7: 1) NV emission dims as the diamond is etched, and 2) the NV emission is completely annihilated after a certain etch depth, depending on the instrument used. The first feature will be discussed in section 4.4.4. We begin our discussion here on the second result, as it shows a difference in NV dynamics when etched in the three reactors.

After etching around 30 nm in the ICP RIE, NV emission is already quenched. Acquiring for longer periods of time or increasing the laser intensity still do not lead to any NV peaks. Once the NV emission is gone, it cannot be regenerated through cleaning or low temperature anneals. Similarly, after 50 nm of etching in the Technics, no NV luminescence is seen. In contrast, after 55-60 nm of etching in the downstream system, the NV signal is still strong. In fact, further etching does not seem to affect the PL emission anymore. We believe this is attributed to roughening of the surface from the etch.
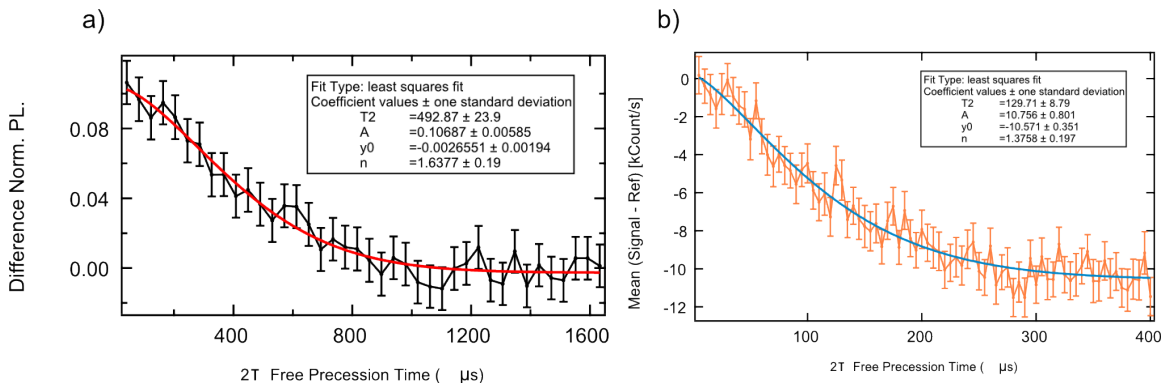


**Figure 4.8:** T2 spin decoherence lifetime fits of NVs in (a) unetched and (b) etched diamond

While the discrepancy between the three systems of when NV emission is eliminated is already notable, further insight can be gained from knowing the actual starting depths of these NVs. The absolute depth of the NVs could vary fairly sig-

64

nificantly, depending on the actual growth rate of the overgrown diamond layer [see section 2.1.2]. After 55 nm of etching in the downstream reactor, the NV signal was still strong. To determine the actual starting depth of the NVs, we relied on spin measurements of the etched NVs. A Hahn echo measurement, taken by B. Myers at UCSB, on several of the etched NVs gave a spin decoherence lifetime, T2, of around 100 $\mu$s [Fig. 4.8b]. Previous studies of these delta-doped samples found that $T_2$ is depth dependent, and 100 $\mu$s corresponds to previously measured NVs $\approx$ 20 nm from the surface.[51] The unetched NV $T_2$ lifetimes measured $\approx$ 500 $\mu$s, in accord to other NVs more than 50 nm deep. It is also known that NVs <50 nm can couple to a bath of electronic spins at the surface ($b_{surf}$), and the measured coupling frequency is strongly depth dependent.[51] In the etched region, the a simultaneous fit of Hahn echo and CPMG-4 coherence decays gave rise to $b_{surf} \approx$ 24 kHz, which again matches previous $b_{surf}$ values for NVs 20 nm from the surface. Assuming that the $T_2$ time has not been affected by our etch, we conclude the initial NVs were likely $\approx$ 70 nm from the surface. This depth is still within the error bars of the initial growth rate.[58]

We can therefore estimate that etching in an ICP RIE reactor with an applied bias will irreparably damage NVs $\approx$ 40 nm from the surface. In contrast, NVs $\approx$ 20 nm from the surface survived in both the photoresist stripper (Technics) and the downstream etcher. It is unclear how close to an NV center a downstream etcher can etch diamond to. Is likely better than the Technics, but that remains to be proven.

There are several potential sources of damage resulting in the quenching of NVs before they are etched away: 1) ion implantation, 2) increased vacancies, and 3) damage from UV light. Ion implantation and vacancy creation is especially problematic

and likely when etching in an ICP RIE. Some preliminary proof of ion implantation from XPS studies is discussed in section 4.5. Creation of shallow vacancies, which have been suggested by another report, are likely to have a significant effect on nearby NVs.[35] In bulk, the charge state of NV depends on nearby substitutional nitrogen atoms, $N_s$, or divacancies, $V_2$, which act as donors and acceptors, respectively.[10] Theoretical experiments have shown that in the regime where $[V_2] < [N_s]$, increasing $[V_2]$ by less than a factor of 2 decreases the $NV^-$ / $NV^0$ ratio by a factor of 100.[10] We did not see any change in the $NV^-/(NV^0+NV^-)$ ratio with each etch step. The $NV^0$ signal decreased in the same trend as shown in figure 4.7. It is possible that the NVs are ionizing into a $NV^+$ state, but this is difficult to prove. And finally, the high energy UV light generated in the plasma has been known to break chemical bonds and generate electron-hole pairs, resulting in the formation of crystalline defects.[31]

### 4.4.4 SIMULATION: NV EMISSION NEAR DIAMOND INTERFACE

From figure 4.7 we also notice that NV dims with etch time with a similar rate, regardless of the instrument. The NV dimming trend can be due to 1) the optics of a dipole approaching a planar interface, 2) the inherent effects of diamond surface on NVs, and 3) damage caused by the etch. The total number of collected photons, N, can be approximated as

$$N = qPN_0\eta = \frac{\gamma_R}{\gamma_R + \gamma_{NR}}PN_0\eta \qquad (4.1)$$

where $q$ is the internal quantum efficiency of the emitter, P is the power emitted per dipole, $N_0$ is the number of emitters, and $\eta$ is the collection efficiency. The internal

quantum efficiency $q$ can be broken down into its radiative and non-radiative decay components, $q = \gamma_R/(\gamma_R + \gamma_{NR})$.

We will first consider the optics of dipole emission and collection, P and $\eta$. Using finite-difference time domain (FDTD) software, we projected the dipole emission in the near-field of the interface into a far-field hemisphere 1 meter away. We simulated the light collected from an objective with numerical aperature (NA) of 0.9 by integrating the field intensity of the far field projection within a 64° cone. Simulation details can be found in Appendix A. As the dipole nears the interface, the far field collected power either increases or decreases, depending on the dipole orientation [Fig. 4.9]. The total power collected follows a similar trend to the simulated radiative decay rate [see Fig. A.3 in Appendix A].
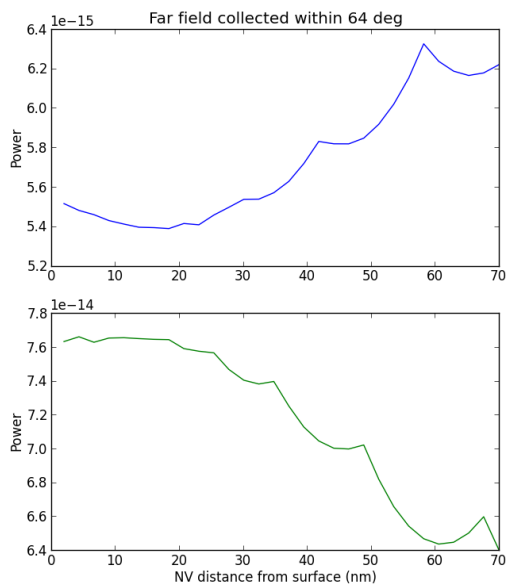


**Figure 4.9:** Power collected within a NA=0.9 objective for a dipole perpendicular (top, blue) and parallel (bottom, green) to the surface.

The NV dipole moment is oriented perpendicular to the NV axis, which is aligned in the (111) crystal lattice direction. Hence, the collected power should be a combination of the effects seen in the perpendicular and parallel oriented dipoles in figure 4.9. Note however the collection of the parallel dipole component an order of magnitude higher, which leads us to believe the majority of the signal should arise from the parallel dipole. Directly comparing results in figure 4.9 to the measured results in 4.7 makes some critical assumptions: 1) the interface is perfectly planar, 2) each NV radiates independently with no superradiance effects, and 3) the incident laser light excites all NVs equally. More simulations are being made to understand the effect of surface roughness, randomly oriented dipoles, and a gaussian laser source on the collected power of the NVs.

Another factor to consider is the correlation between NV dynamics and its distance from surface. From the AFM, we noticed the diamond is quite pitted [Fig. 4.6a]. Therefore, etching likely not only etches from the top, but also laterally in the pits, further increasing the likelihood that select NVs are near surface. This is an area that is not well-understood. A report NVs implanted at various depths showed that NV luminescence decreases when NVs are implanted closer to the surface.[56] But it is unclear if that is an inherent property of how the surface affects NVs or if it is due to a lower conversion efficiency in the implantation process. Delocalized image states, deep sub-bandgap states related to surface-termination, and localized acceptor states near surface are theorized to lead to photobleaching and blinking.[33] It has also been demonstrated that a thin layer of diamond overgrowth increases the $T_2$ spin decoherence lifetime of implanted near-surface NVs, further proving the presence of

the surface itself is a problem.[79] These surface could ionize the $NV^-$ state, which would decrease the number of emitters, $N_0$, or increase the non-radiative decay rate $\gamma_{NR}$. Changing both of these values result in a lower measured NV intensity, according to equation 4.1.

Finally, plasma damage would also affect both $N_0$ and $\gamma_{NR}$. It is possible that, while the downstream etcher is less damaging than the other systems tested, it still creates vacancies or other defects, thereby reducing the number of emitters, $N_0$. Vacancies or ions implanted and diffused through the lattice from the plasma can annihilate or ionize NV centers, as discussed in section 4.1. However, if the effect of $N_0$ due to damage is significant in the first 20 - 30 nm of etching, then the slope in figure 4.7 should be different between the downstream and ICP RIE experiments. Unfortunately, the error bars are too large to elucidate any significant differences in slope.

In conclusion, the dimming of NVs is likely due to a combination of dipole emission properties when in the near-field of the surface, and the inherent effects of surface on NVs. We have shown that an oxygen plasma in ICP RIE system can be damaging to near-surface NVs. NV emission dies out after a cumulative 120 seconds of etching, when the NVs are still 40 nm from the surface. In contrast, NVs brought closer to the surface with the downstream reactor survived longer. However, downstream etching is not suitable for etching more than 10 nm of diamond, as it roughens the surface considerably. In order to probe the true limits of downstream etching, we need to repeat the experiment on sub-10 nm deep and single NVs.

## 4.5 XPS studies of damage

In addition to gauging the health of NV centers through measuring their luminescence, we used high resolution XPS to gain some material insight to the surface chemistry.

### 4.5.1 Embedded Chlorine

Argon-Chlorine is a common combination of gases that etch diamond. It has a slower etch rate than O2 plasma, and is more isotropic. However, it was been known to cause nearby NV emission to disappear.

A single-crystal diamond was exposed to 3 min of $Ar/Cl_2$ plasma at a DC bias of 250 V in an ICP RIE, followed by 30 sec of $O_2$ in the same system (see table 2.1). 30 seconds of $O_2$ plasma etches approximately 60 nm of diamond, more than enough to remove any chlorine-termination. To remove any adsorbed chlorine that may have deposited from the reactor chamber walls, the sample was then removed from the ICP RIE and placed in a separate reactor (Technics). We etched the sample for 15 min, which should remove at least a few nanometers of diamond while also cleaning the surface.

An XPS survey scan of the sample post-processing showed no chlorine peak. However, taking a high resolution scan of the Cl 2p peak resulted in a small peak [Fig. 4.10]. Diamonds not previously treated in chlorine plasma do not show the same peak. Since about 60 nm of diamond should have been etched away by the 30 seconds of oxygen plasma in the ICP and the 15 min of barrel etch, we roughly estimate that the chlorine ions have channeled as far as 60 nm deep from the surface. This suggests that chlorine could be implanting into the diamond, explaining why near-surface

70

NVs rarely survive from etches chlorine-based etches. More rigorous study needs to be made to prove this hypothesis.
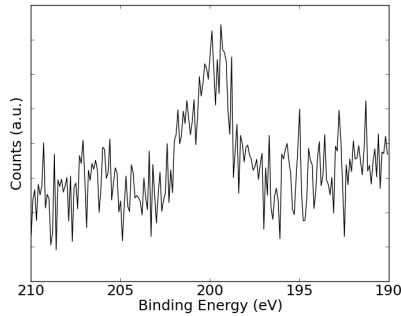


**Figure 4.10:** Chlorine peak evident in XPS after etching the sample in oxygen plasma following a chlorine plasma treatment.

### 4.5.2  BINDING ENERGY OF $sp^3$ C-C DUE TO $SF_6$ PLASMA DAMAGE
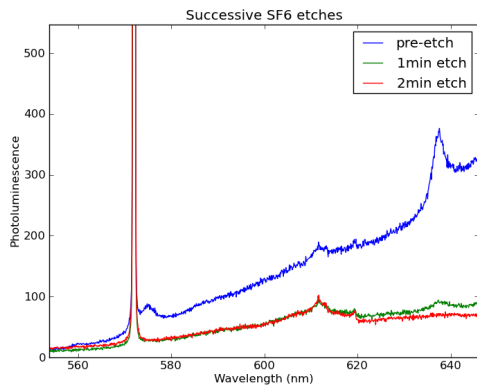
**(a)** ICP RIE                                              **(b)** downstream etcher
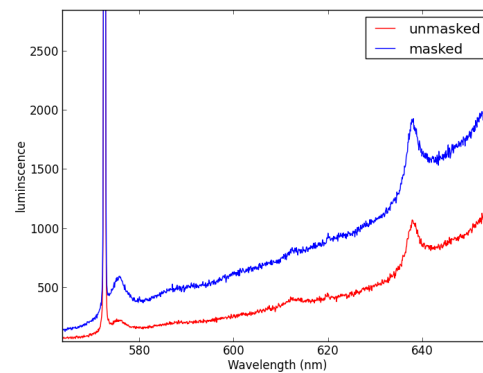


**Figure 4.11:** NV luminescence dimming with $SF_6$ plasma with two different etch systems.

As was alluded to in chapter 3, the most reliable fluorination with $SF_6$ was achieved with a downstream ashing system. Using a sample with implanted NVs $\approx 15$ nm from

the surface, we etched away a small amount of diamond with $SF_6$ plasma. Figure 4.11 compares the NV photoluminescence intensity after etching $\approx$2 nm from the surface in an ICP RIE and downstream system. The diamond etched in the ICP RIE resulted in no more NV emission, whereas NV emission is only dimmed in the downstream case.

We studied the diamond surface chemistry in the XPS. The survey scan of the diamond treated with $SF_6$ plasma in the ICP RIE showed 91% carbon, 8% fluorine, and 1% oxygen. Interestingly, we found the main peak in the C 1s high resolution scan, which should correspond to $sp^3$ C-C, consistently shifts to be around 1.5 eV higher [Fig. 4.12]. Furthermore, the main peak broadens compared to an untreated, boiling acid cleaned diamond. While the peak nearly coincides with where C-O is normally found, the low oxygen signal means the largest fraction of carbons cannot be oxidized carbon. It cannot be due to charging because the lowest peak is more than 2.7 eV lower in binding energy, which is too large of a splitting between $sp^3$ and $sp^2$ C-C binding energy. The C 1s high resolution of a sample etched in the downstream reactor, in contrast, shows a main peak that overlaps directly with the untreated, oxygen-terminated surface.

A similar shift in the $sp^3$ bulk signal has been reported previously, and was attributed to lattice damage of $Ar/O_2$ plasma on boron-doped diamond.[11] We therefore conclude that the shift the main C 1s peak could be attributed to a damaged layer within the surface, caused by implanted fluorine. Similar to the XPS data from $CF_4$-treated surfaces, but here the C-CF bond exists within the diamond lattice instead of as a deposited polymer on top of the surface, which acts as a protective layer.
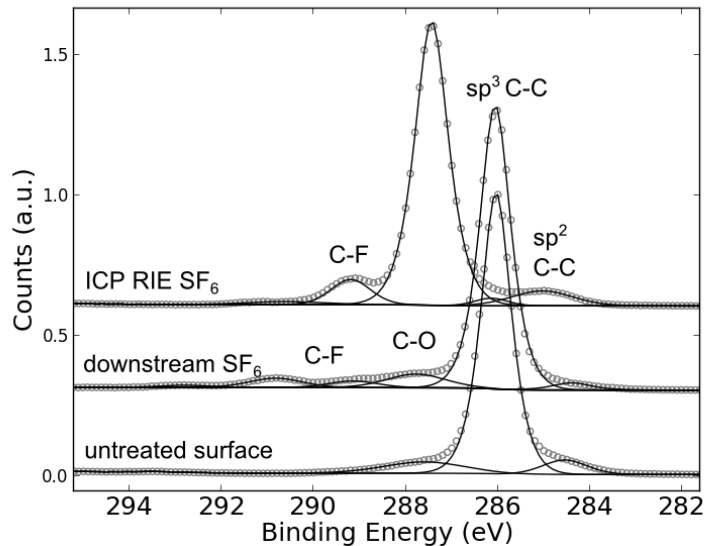
**Figure 4.12:** High resolution carbon scan of a diamond cleaned with boiling triacid, and fluorine-terminated with $SF_6$ in either a downstream reactor or an ICP RIE reactor. The sample etched in a ICP RIE has a significantly shifted main peak, which is likely due to lattice damage from the etch.

## 4.6 Conclusion and Outlook

In this chapter we explored the effects of etching diamond in $H_2$, $O_2$, $Ar/Cl_2$, and $SF_6$ gases in three types of reactors: ICP RIE, barrel reactor, and downstream asher. We found that very shallow etches in $H_2$ plasma affect NVs 70 nm deep, despite using milder conditions than reported in literature. Finally, we demonstrated that oxygen plasma etching in ICP RIE or even barrel reactors damage NVs. The least damaging method for thinning diamonds, is a downstream set-up. Sources of plasma damage include ion implantation, increased vacancies from high energy ions, and crystal defects from UV light. Some preliminary studies of the surface material with XPS suggest that implantation could be a source of issues. If the ions are implanting

73

$> 60$ nm deep, we can imagine vacancies created by the physical sputtering are also created and diffused into the substrate. Potentially, a combination of vacancies and implanted ions contribute to a shifting of the $sp^3$ C-C peak, as seen in diamonds damaged by $SF_6$ plasma.

In addition to damage, we also explored the effect of NV emission due to the surface. NV emission, independent of the etch system used, dims as it nears the surface. It is still difficult to decouple the different sources of this dimming, but we believe that surface states play a major role.

Future studies of NV dynamics as a function of its distance to the surface is best carried out in a downstream reactor with delta-doped single NVs closer $< 20$ nm from the surface. We need smoother, non-pitted surfaces to start out with as not to complicate the distance-to-surface measurements. And finally, a more thorough material study of the damage mechanism is needed to truly understand the effects of plasma damage.

# 5

# Diamond-plasmonic hybrid cavity

So far, we have focused our discussion on how to change surface terminations to increase NV emission (chapter 3) or how to bring NVs closer to the surface while minimizing NV emission loss (chapter 4). In this chapter, we look to increase NV emission by orders of magnitude by addressing two fundamental and significant issues with using NVs as an emitter. One, the extraction efficiency in bulk diamond is

around 3% due to diamond's large refractive index. Two, the branching ratio, defined as the emission into the zero-phonon line (ZPL) over the vibrational bands, is also around 3%. To increase the collection of NV emission, bulk diamond has been shaped into solid immersion lenses and[22] waveguiding nanowires.[26,2] Both structures boast an order of magnitude improvement of the collection efficiency. Extraction can be further improved with a metallic grating around the emitter.[7] However, the most important feature of the NV emission is the ZPL, and an engineered optical cavity is the best way of increasing both the branching ratio and the extraction efficiency. Here we explore a new design that confines light near the surface of the diamond to enhance near-surface NV$^-$ ZPL emission.

## 5.1 OPTICAL CAVITY ELECTRODYNAMICS

An optical cavity can most simply be described in a classical manner as light reflecting between mirrors and forming standing waves at certain frequencies, called resonance modes. The dimensions of the cavity controls the frequency of the modes. Optical cavity systems can also be described quantum mechanically as a perturbation of an emitter transition. Fermi's golden rule [Equation 5.1] states the transition probability of an emitter decay ($\gamma$) depends on the dipole interaction with the electric field, and number of ways the transition can happen (ie. density of states).[54]

$$\gamma = \frac{2\pi}{\hbar}|\langle f|\hat{H}_I|i\rangle|^2\rho \tag{5.1}$$

$\hat{H}_I = -\hat{\mu} \cdot \hat{\mathbf{E}}$ is the interaction Hamiltonian between the dipole, $\hat{\mu}$ and the local field $\hat{\mathbf{E}}$. The interaction Hamiltonian tells us that a high emission rate is achieved

76

when the dipole is spatially placed in the field maximum, and the dipole is oriented along the electric field.

Equation 5.1 also states that a higher density of states, $\rho$, leads to faster emission decay. In a homogenous medium, $\rho$, the local density of optical states (LDOS) depends on the refractive index (n) of the material. Hence, the spontaneous decay rate at frequency, $\omega$, is:

$$\gamma_R = \frac{1}{\tau} = \frac{\omega^3 n |\mu|^2}{3\pi \epsilon_0 \hbar c_0^3} \tag{5.2}$$

where $\mu$ is the dipole moment, $\epsilon_0$ is the vacuum permittivity, $\hbar$ is the reduced Planck constant, and $c_0$ is the speed of light in vacuum. In a cavity, LDOS is enhanced at the cavity resonance modes and suppressed at frequencies outside the modes, thereby influencing the final state into which an emitter decays. An optical cavity can be engineered such that its resonance modes overlaps with the ZPL frequency. The NV emission is thus far constrained such that it emits preferentially into the ZPL. The extraction efficiency can also be influenced by the shape of the cavity.

The goal of our cavities is to increase the radiative emission rate into the ZPL. The figure of merit, Purcell factor, describes the enhancement of the spontaneous emission rate in the cavity, $\gamma$, over its rate in vacuum, $\gamma_0$. The Purcell factor can be derived classically or from Fermi's golden rule, and is most commonly seen in the following form:

$$F_P = \frac{\gamma}{\gamma_0} = \frac{3}{4\pi^2} \left(\frac{\lambda}{n}\right)^3 \left(\frac{Q}{V}\right) \tag{5.3}$$

where $\lambda$ is the wavelength of the mode, n is the material index of refraction, Q is the cavity quality factor, and V is the modal volume. The cavity Q describes how long

the light can remain trapped before leaking out, through non-radiative pathways or scattering into the air due to fabrication imperfections. It can be measured from the mode frequency ($\omega$) and its full-width half-max ($\Delta\omega$):

$$Q = 2\pi \times \frac{\text{Energy stored in cavity}}{\text{energy lost per cycle}} = \frac{\omega}{\Delta\omega} \tag{5.4}$$

Equation 5.3 tells us that for a given wavelength, the enhancement of the spontaneous emission rate depends on how confined the light is in the cavity (high Q) and how small the mode volume is.

Various all-diamond cavities have been fabricated to increase NV emission. Cavity geometries that have been successfully realized include micro-ring resonators,[16] one-dimensional photonic crystal nanobeams,[66] and two-dimensional photonic crystals.[17] The highest measured Q of an all-diamond cavity near the NV ZPL thus far has been 24,000 (to be published from our group). However, the modal volumes in these dielectric cavities are diffraction limited, which limits the Purcell factor. Plasmonic cavities have been demonstrated to achieve enhancements higher than those in dielectric cavities, despite having a lower Q factor.[71] In this chapter, we will first explore the Purcell enhancement in a cavity based on an emitter near a flat metallic surface.

## 5.2 Gap mode plasmonic cavities

In chapter 4, we simulated the effect of a dipole, embedded in bulk diamond, approaching a planar interface with air. Similarly, we can consider the decay rate of a dipole in air approaching a metal interface, as first demonstrated by Drexhage.[15]
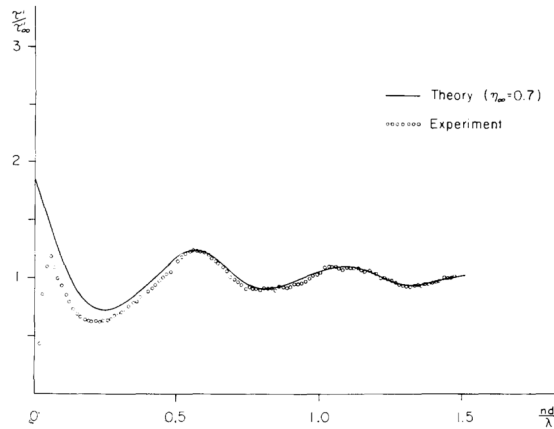
**Figure 5.1:** Lifetime of $Eu^{3+}$ emitter near a silver surface, figure from Ref. 15

Figure 5.1 shows the theoretical and experimental results of the $Eu^{3+}$ emitter lifetime, normalized by its lifetime in air, in the presence of a silver mirror. Oscillations in the emission lifetime are due to constructive or destructive interferences of the dipole field and field reflected from the surface of the mirror. The amplitude of the oscillations is heightened as the dipole approaches the metal, because the fields interact more strongly. When the dipole is very close to the surface, Drexhage noticed that experimentally the emitter lifetime rapidly falls off whereas the pure radiation model leads to a rise in lifetime. We now know that at these distances, the dipole fields are coupling to evanescent field components, including surface plasmon polaritons (SPPs). A SPP is a collective oscillation of electrons at the surface of a metal, which can be described as a highly localized electromagnetic wave propagating at the metal-air interface.

The high field intensity near the metal surface decreases the radiative lifetime ($\tau_R$), which increases the emitter intensity. However, metals also have many lossy channels, which decrease the non-radiative lifetime ($\tau_{NR}$). Confining the dipole in an optical

79

cavity increases the LDOS by coupling the SPP to a cavity mode, and selectively decreases $\tau_R$ over $\tau_{NR}$, such that the dipole emission is not simply quenched.

### 5.2.1 Diamond plasmonic cavity

When two metal surfaces are brought together, a hot spot of high electric field can be created in the gap. Broadband emission rate enhancement has been demonstrated in NVs between two gold nanoparticles,[74] silver nanowires.[38] These structures are taking advantage of the enhanced near field of the metals, and the structures are considered antennas, not cavities. In antenna structures, the modal volume (V) is low, but the quality factor is also low ($<10$).

A diamond plasmonic cavity, with a measured Q of 58, has previously been fabricated by coupling nanodiamonds to silver nanowires with patterned dielectric reflectors.[9] A plasmonic cavity based on bulk diamond has been fabricated, with a simulated and measured Q of 150 and 10, respectively. The design is composed of a silver aperture around a diamond nanorod, encompassing a single NV.[7,8,5] A Purcell factor of around 6 was observed. The measured Q factors of diamond plasmonic cavities have all been very low, most likely due to lossy channels in metals.

High electric fields can be confined in the low-index gap between a high index material and a metal surface. Oulton *et al* simulated a high-index (GaAs, n = 3.5) nanowire approaching a silver substrate, and found a highly confined field in the gap, due to the hybridization of the dielectric waveguide with the surface plasmon mode.[60] This hybrid mode has a long propagation length because the field is away from the metal and has been used to make a plasmon laser.[61]

Owing to diamond's high dielectric constant (n=2.4), we propose a hybrid diamond-plasmonic cavity, where we hybridize a diamond cavity with surface plasmons on a silver surface. This results in a relatively high Q (around 250) cavity where the electric field is confined in a thin gap of low-index material between the diamond and silver mirror. By separating our diamond from the silver with a low-index material, our cavity is designed have a higher Q factor than previously proposed diamond plasmonic cavities, whose Qs cap off at 150.[5]

## 5.3 CAVITY DESIGN



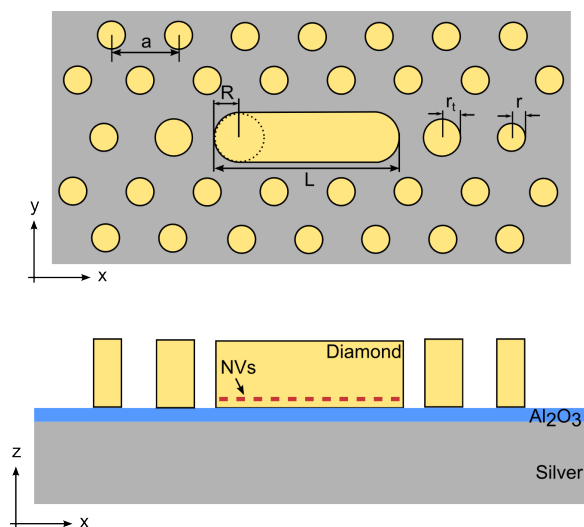**Figure 5.2:** Top down and cross-sectional view of our hybrid plasmonic-photonic crystal cavity.

Our hybrid cavity is specifically designed to enhance the emission of near-surface NVs by coupling those NVs to enhanced fields near the diamond surface. Our cavity is composed of a 2D photonic crystal made of high index dielectric rods (diamond), a small gap of low index dielectric (alumina), and a silver substrate [Fig. 5.2]. The

81

photonic crystal made of periodical hexagonal rod structures hybridizes with the surface plasmon modes to create a highly concentrated TM mode in the low index gap. A cavity is formed by introducing a linear defect to create a standing wave (cavity mode) with resonance within the photonic band gap. A detailed discussion of the cavity structure and simulations can be found in reference 43, where the emitter was placed in the middle of the low-index gap. The simulated Q with an emitter in the middle of the gap was around 300.
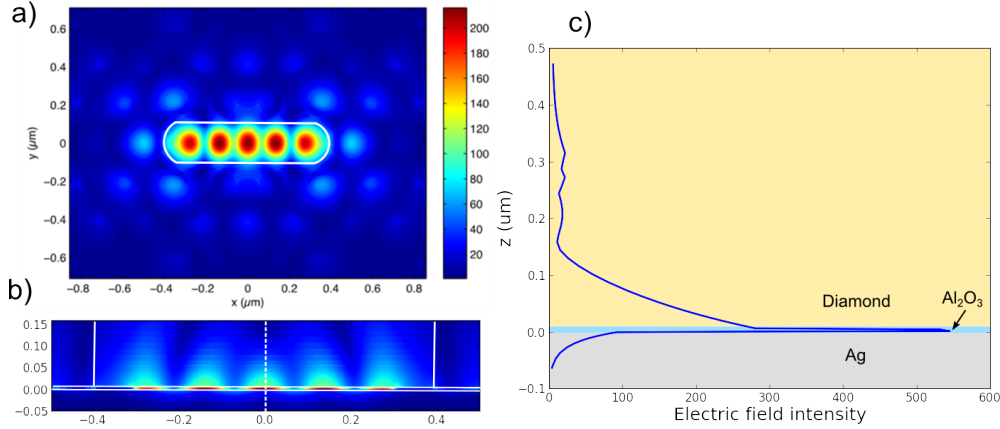


**Figure 5.3:** Cavity mode profile, centered at 636 nm, in (a) top down view (defect region highlighted in white), and (b) cross-sectional view (material boundaries with white lines). The electric field along the dashed line is plotted in (c), showing high field confinement in the gap. Simulation data courtesy of X. Zhang.

We used finite difference time domain simulations (FDTD, Lumerical) to model the cavity. An electric dipole oriented perpendicular to the interface was placed 10 nm from the diamond-alumina boundary. Diamond rods, n=2.4, were simulated with a height of 600 nm, radius (r) of 66 nm, and lattice constant (a) of 230 nm. These parameters define the band-gap energy, within which cavity modes can lie. The defect consisted of 3 conjoined rods (L3) of radius R, such that the length of the cavity L =

2R + 2a. R was varied between 1.2r to 1.5r to tune the cavity mode frequency. Below the diamond was a 5 nm thick $Al_2O_3$ layer, and a silver substrate. The electric field profile of a resulting cavity mode, centered at 636 nm, is shown in figure 5.3. The field is highly confined in the low index spacer layer, but NVs within the top 50 nm can still couple into the mode relatively efficiently [Fig. 5.3c]. The mode frequency can be further tuned by adjusting the defect size, R. The cavity Q and far field radiation can be increased by adjusting $r_t/r$ ratio. The freedom allowed by this two-dimensional photonic crystal allows us to both maximize the extraction efficiency of NV emission and the branching ratio of the NV ZPL.

## 5.4  FABRICATION

The fabrication of our plasmonic photonic crystals (pphCs) is outlined in figure 5.4, and was designed by Dr. Tsung-li Liu. The first five steps of how these thin diamond membranes are created and bound have been covered in section 2.3. We first select samples where the overgrown layer (200 nm thick) has no detectable NVs, and we then implant $^{14}N$ at 6 keV and $10^{13}$ ions/cm$^2$ to create NVs $\approx$ 10 nm from the surface.
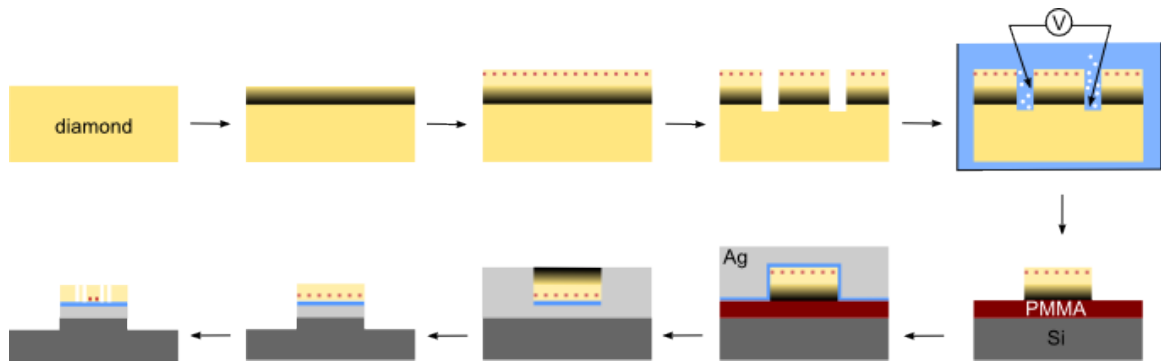


**Figure 5.4:** Fabrication process for the hybrid plasmonic photonic crystal.

To bind the membrane onto a planar substrate, we spin C6 poly(methyl methacrylate) PMMA at 3000 rpm for 40 seconds onto a clean silicon piece. We then press the membrane into the PMMA layer with the near-surface NV side facing up, and attach the membrane into position by baking the silicon piece at 180°C for 1 min. We then deposit 5 nm of $Al_2O_3$ in an atomic layer deposition system (ALD) at 50°C, and 250 nm of silver in an electron-beam evaporator.

Next, the sample needs to be flipped onto another silicon substrate, which is accomplished through a process called "template-stripping."[52,28] This method has been used previously in for creating ultra-smooth silver surfaces for nanowire cavities and making silver-trench cavities.[72,42,83] We attach another silicon handle on top of the silver with room temperature epoxy (EPO-TEK), which takes 24 hours to cure. During this process, the epoxy binds the silver and diamond membrane to the second silicon handle, and the whole sample can be flipped by sliding a razor blade under the deposited silver to remove the PMMA and initial silicon sample.
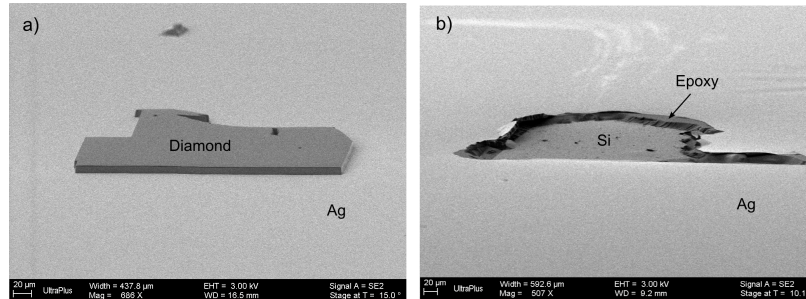


**Figure 5.5:** SEM at 80° tilt of (a) a successfully template-stripped and etched membrane, and (b) an unsuccessful template-strip, where the diamond was bound too tightly to the PMMA.

The failure rate of this template-stripping step was surprisingly high because there is a trade-off between achieving a flat membrane in the binding process and

successfully template-stripping the membrane off with the silver. A strong bond between the PMMA and diamond produces a flat diamond membrane. A convex or concave diamond often only makes a few points of contact to the PMMA and is easily lost during subsequent processes. However, if membrane is bound too tightly, the template stripping only removes the silver from the top of the diamond, whereas the membrane itself stays on the PMMA. In figure 5.5b, a scanning electron microscope (SEM) image shows template-stripped silver with a void where the diamond should have been. The membrane was left on the first silicon wafer, attached to the PMMA. It is thus important to minimize the heating of PMMA to prevent over-curing it.

Once a membrane has been successfully template-stripped, the damaged, over-grown layer of the diamond membrane is etched away in the inductively-coupled reactive ion etcher (ICP RIE) with a 15 min $Ar/Cl_2$ etch and 2-4 min of high bias $O_2$ plasma (etch rate $\approx$ 160 nm / min, detailed process conditions described as Process #1 and 2 in table 2.1), leaving a diamond layer approximately 300 - 600 nm thick. The resulting membrane can be seen in figure 5.5a.

We pattern a 2D photonic crystal with electron-beam lithography. A 15 nm titanium layer was evaporated on the diamond as a conductive layer, and to improve the adhesion to the e-beam resist. We spin-coated hydrogen silsequioxane (HSQ), a negative e-beam resist, at 3000 rpm for 40 seconds, and baked it at 180°C for 5 min and 120°C for 5 min. After exposure, the resist was developed in tetramethylammonium hydroxide (TMAH). The resulting pattern can be seen in figure 5.6a and b.

Finally, the resist pattern is transferred into the diamond using a 20 second ICP RIE etch in $Ar/Cl_2$ to remove the thin Ti layer, and 1-3 min of high bias $O_2$ plasma
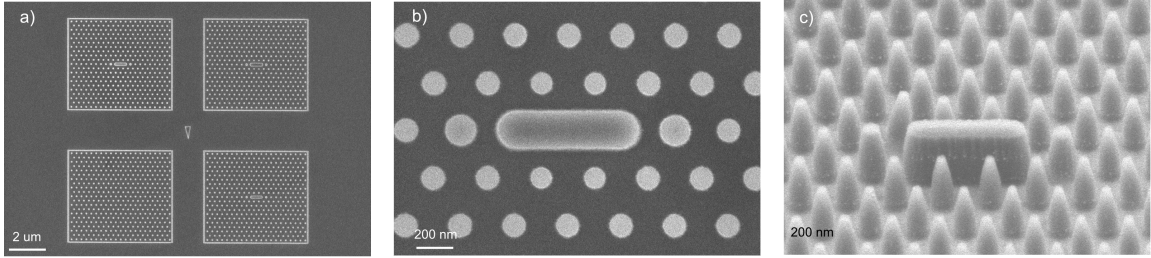
**Figure 5.6:** SEM of the hybrid plasmonic photonic device. (a) Top down view of four photonic crystals, one with no defect (bottom left), and three with different size defects. (b) Top down view of the defect regions. (c) A 45 degree view of the etched device.

to etch the diamond. The resulting structure is seen in figure 5.6c.

A challenge in these process steps is determining the membrane thickness before patterning the device, which is crucial for several reasons. One, the thickness of the structure determines the wavelength of the mode, which will be discussed later. Membranes less than 200 nm have been found to be too thin to support modes. Two, knowing the thickness gives us an estimate of how far to etch when transferring the pattern. The 5 nm of $Al_2O_3$ below the diamond can act briefly as an etch stop layer, but not for long. Etching through the alumina layer with the $O_2$ plasma instantly oxidizes the underlying silver layer, and dramatically changes its optical properties and prevents the formation of plasmonic gap modes.

Usually, at a high-tilt SEM image, the boundary of diamond and the binding material (PMMA or epoxy) can be seen, and a thus the diamond thickness can be estimated. However, because silver is sputtered and easily redeposited on the side walls of the diamond, the boundary is no longer visible. We thus rely on using a focused-ion beam (FIB) to micromachine a $2 \times 3$ $\mu$m hole to determine the thickness (figure 5.7). The boundaries between the materials can be easily distinguished and

86

an SEM is then used to measure the diamond thickness.
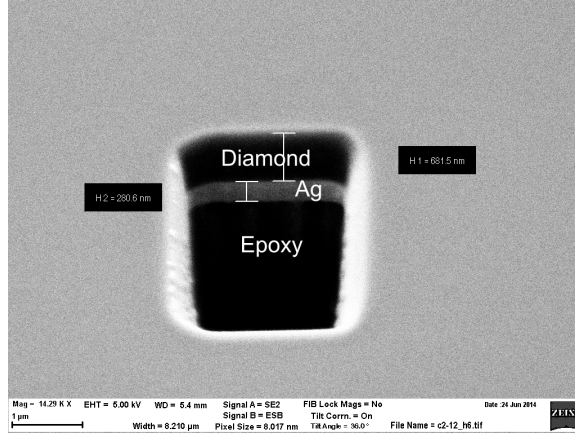


**Figure 5.7:** Determening the diamond thickness with a tilted SEM image of a hole created with FIB.

Using the initial diamond membrane thickness, we carefully transfer the pattern in the ICP RIE, until the diamond rod height matches the initial measurement, and the diamond is etched through.

## 5.5  RESULTS

Optical measurements were taken at room temperature in our home-built confocal set-up [Fig. 2.5]. A bright undecorated NV signal is seen from the photoluminescence of a defect-less photonic crystal. When illuminating a crystal with an L3 defect, we find a prominent mode that rises above the NV background [Fig. 5.8a]. From the simulations, we expect the mode to be linearly polarized parallel to the direction of the L3 defect. Thus some of the background fluorescence uncoupled to the polarized mode can be filtered out by placing a polarizer is before the spectrum analyzer, and tuning it to the axis of the defect [Fig. 5.8b]. Turning the polarization by 90 degrees

results in a spectrum consisting only of background luminescence. The highest Q measured is $\approx 170$, not far from the simulated Q of $\approx 200$. This is the highest Q observed in a diamond-plasmonic cavity.
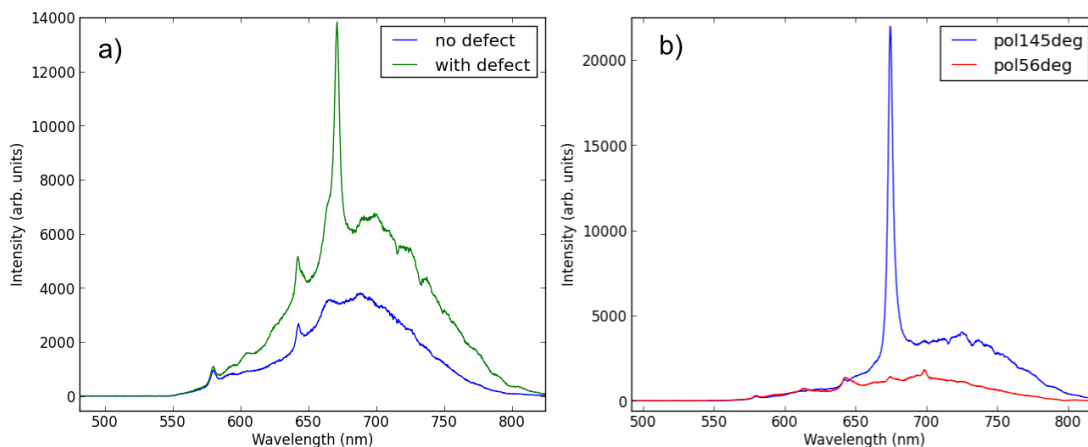


**Figure 5.8:** NV emission decorated with a cavity mode, shown in (a) to only exist in a photonic cavity with a defect, and in (b) to be linearly polarized along the axis of the defect. The Q measured is ~170.

In order to ultimately measure an increase in the spontaneous emission rate of the NV$^-$ ZPL, we need to tune the cavity mode into resonance with the NV$^-$ peak. The mode wavelength is controlled by the photonic crystal spacing, the rod radius, and the cavity size. In figure 5.9a, the cavity mode sequentially red-shifts from 716 to 729 nm as the L3 defect radius, R, increases from 1.2r = 79.5 nm to 1.5r = 99.4 nm. Red-shifting can also be irreversibly achieved by depositing thin layers of oxide on the device with atomic-layer deposition.[72] Blue-shifting was observed in our cavities by etching more of the diamond, and decreasing both the rod size and the cavity. Figure 5.9b illustrates the photoluminescence of the mode of the same structure with sequentially longer etch times. One needs to careful of this method, as it is easy to

over etch the device and tarnish the underlying silver layer. It can be seen that after etching for 2 min and 20 seconds, the Q of the mode has decreased, likely due to some damage to the silver. Any roughening of the silver surface results in higher losses and poor sustenance of surface plasmon modes.
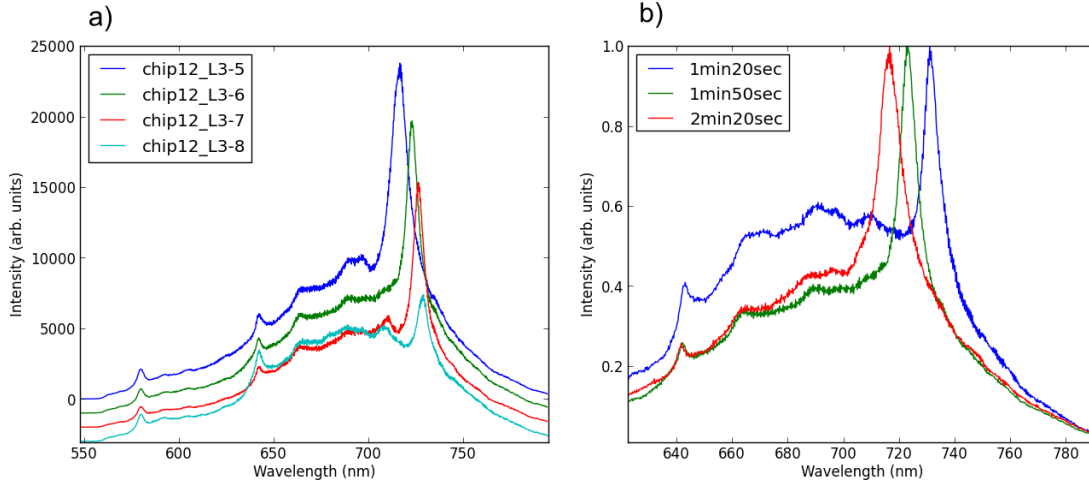


**Figure 5.9:** Mode tuning achieved by (a) changing the defect size, and (b) etching the diamond for longer time to decrease the photonic crystal rod radius.

Proof of Purcell enhancement is usually found through measuring the emitter lifetime inside and outside the cavity. Using a super continuum laser with rate of 76 MHz, we collected a time-resolved distribution of photon counts with an avalanche photodiode (APD). These lifetimes are derived from a mono-exponential fit of the emission decay. The first 3 ns are skipped to avoid any influence of the fast decay paths from any contamination on the sample. Representative lifetime plots are shown in figure 5.10.

The lifetime of NV in bulk diamond ($\tau_{bulk} = 13$ ns) decreases compared to $1 \times 1\ \mu$m square diamond on silver ($\tau = 8.9$ ns), due to quenching from the metal surface. As
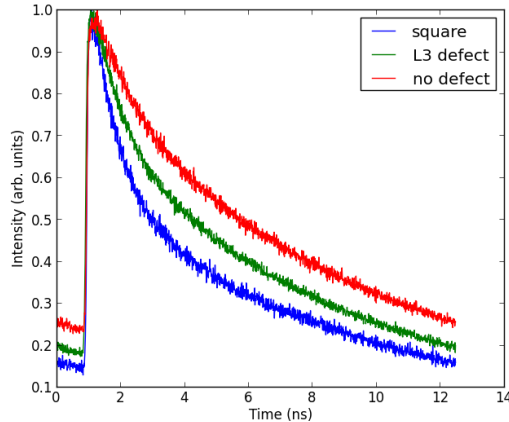
**Figure 5.10:** Lifetime of ensemble NVs in a $1 \times 1$ $\mu$m square, in a L3 defect, and in a photonic crystal with no defect.

discussed earlier, the non-radiative emission decay rate of an emitter ($\gamma_{NR}$) increases with proximity to a metal. The lifetime of cavity is approximately the same ($\tau_{defect}$ = 8.7 ns). The lifetime of a plasmonic photonic crystal without a defect is slightly longer ($\tau_{nodefect}$ = 9.7 ns). There are two reasons why $\tau_{defect} < \tau_{nodefect}$. One, since a photonic crystal with no defect has a smaller effective index compared to one with a defect, it experiences a slower decay rate ($\gamma$) or higher lifetime. Two, the enhanced fields and LDOS at the wavelength increases the emission rate of the emitter in the dipole, as was discussed in equation 5.1.

No significant Purcell factor was observed. We believe there are several issues at hand. One, we used an unusually high NV implantation density, which means the large ensemble NVs have a lot of straggle in depth. The large NV background suggests many of the NVs are not coupled to the mode. Furthermore, our modes are all quite red-shifted from the NV$^-$ ZPL. A more accurate Purcell measurement should be made at low temperature and through tuning the mode to resonance with

the NV⁻ ZPL.[16]

## 5.6 Conclusion

We present here a proof of concept of a new hybrid cavity structure designed to selectively enhance near-surface NVs. We fabricated the device and measured a Q of 170, the highest Q reported for a diamond-plasmonic cavity. The small modal volume from the hybrid photonic crystal and plasmonic fields should give us high Purcell factors, when the mode is tuned in resonance with the NV⁻ ZPL. Future experiments include fabricating these devices on thinner diamond membranes to create modes closer to the ZPL. Furthermore, we will use a lower NV density and bring them closer to the diamond surface for better coupling to the high electric fields.

# 6
# Conclusion and Outlook

The nitrogen-vacancy center (NV) has many promising applications, and has generated much excitement in the physics, biology, and chemistry communities. The number of papers published about the nitrogen vacancy center has quadrupled in the past 5 years. The combination of optical read out of spin, and the robustness of diamond, makes the NV center an impressive system. Yet, as scientists work to

create magnetometers with higher sensitivities, emitters with higher efficiencies, and qubits with longer spin memories, they all recognize how sensitive and fragile the NV system is. Specifically, when the NV is less than $\lambda/n$ from the surface, extra care is needed in fabricating the surrounding diamonds.

In this work, we have shown various ways of stabilizing and destabilizing the emission of near-surface NVs. We probed the only surface chemistry, and found that oxygen-termination leads to NV properties that degrade over time. A polymerized fluorocarbon layer may stabilize those near-NVs more effectively than oxygen does. We also established how sensitive NVs are to dry etching, an unavoidable part of NV-based devices. Parameters to consider include the choice of gas ($Cl_2$ and $H_2$ are especially damaging), DC bias, etch time, chuck temperature, and reactor geometry. Based on our results, we proposed using a downstream system to etch the last 10-20 nm of diamond, as the NV gets closer to the surface. We also suggest that NV luminescence, potentially independent of plasma damage, becomes dimmer as its distance to the surface decreases. Finally, we demonstrated an optical cavity that specifically enhances near-surface NVs, with the highest diamond plasmonic cavity Q.

The biggest obstacle with this research, and all diamond surface-related research, is that it is a complicated system with many variables that are difficult to decouple. When "surface effects" are cited for diminishing NV properties, they could be referring to band bending due to surface adsorbates, localized surface acceptor states, chemical binding and termination at the surface, surface reconstruction, and subsurface crystalline defects in forms of implanted foreign atoms or vacancies. Furthermore,

the effect of all these properties on NVs depends on the NV distance from the surface.

Further understanding of the surface effects on nearby NVs is crucial for the next stage of NV research. There are a few areas of study in particular that would benefit the community. For once, it would be interesting to truly isolate the effect of NV distance to surface, which would benefit from delta-doped single NVs <10 or 20 nm from the surface. The downstream etcher proposed in this work is a good starting point, as a way of minimizing plasma damage. Two, tuning the mode of our diamond plasmonic cavity into resonance with the zero-phonon line of the NV allows us to better estimate the lifetime enhancement. It is important to extrapolate some of our ensemble emission results to other NV properties, such as spin decoherence lifetime, zero-phonon line linewidth, NV emission dynamics (ie. stability).

# A

# Dipole near planar interfaces

Dipoles more than a few wavelengths into a bulk material can be considered to live in a homogeneous system. The radiative emission decay rate is simply calculated with equation A.1 and collection efficiency can be extracted from ray optics. However, when a dipole is less than a wavelength from the surface, we need to take into account the fields reflected and refracted from the interface.

We assume a dipole is embedded in medium 1 near an interface with medium 2. Both mediums are homogeneous and lossless dielectrics with refractive indices $n_1$ and $n_2$, respectively. We define the relative index, $n$, as the ratio of $n_2/n_1$. In our simulation, $n_1 = 2.4$, and $n_2 = 1$, and thus n <1. We model a dipole perpendicular and parallel to the interface, at a distance $z_0$ [Fig A.1]
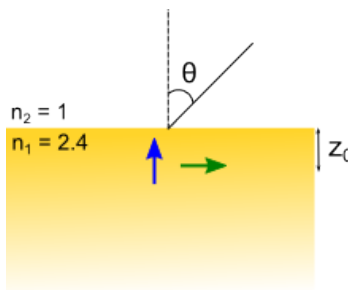


**Figure A.1:** Simulation schematic

## A.1   DIPOLE POWER

The power emitted by the dipole depends on the interaction with its emitted field and the reflected field from the surface[47]. The oscillation of a dipole was decomposed into s- and p-polarized plane and evanescent waves. The reflected waves were calculated from the reflection coefficients. Both the plane and evanescent waves emitted from the dipole create interferences which affect the total power emitted by the dipole. The total power emitted by the dipole is normalized for the power emitted in a homogenous medium 1:

$$P_0 = \frac{m_0^2 \omega^4 n_1^3}{12\pi\epsilon_0 c^3} \tag{A.1}$$

We can approximate the dipole power $(P/P_0)$ when $z_0 > \lambda_1$ by using the equations

from reference[47].

$$[P/P_0]_\perp = 1 + 3\frac{n-1}{n+1}(\bar{z}_0^{-3}sin\bar{z}_0 - \bar{z}_0^{-1}cos\bar{z}_0) \qquad (A.2)$$

$$[P/P_0]_\parallel = \frac{1}{2}(1 + P_\perp/P_0) - 3\frac{n-1}{n+1}\bar{z}_0^{-1}sin\bar{z}_0 \qquad (A.3)$$

where $\bar{z}_0 = 4\pi z_0/\lambda_1$.

We plot the results of the analytical model in figure A.2. The oscillations originate from the interference between the propagating fields of the dipole and the reflected fields from the surface.
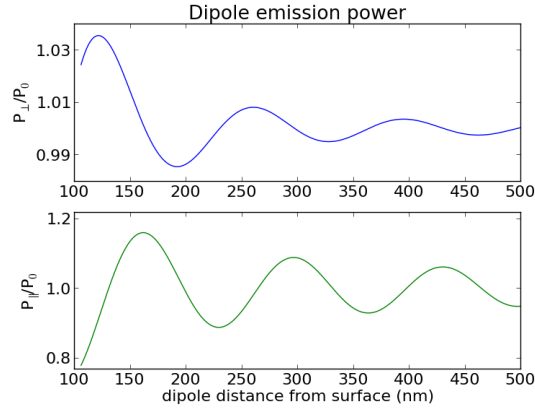


**Figure A.2:** Analytical solution to the total emitted power of a dipole, when $z_0 > \lambda_1$.

When the internal quantum efficiency, defined as the ratio of radiative decay to total (radiative and non-radiative) decay, equals 1, $P/P_0 = \gamma/\gamma_0$. Thus, the power emitted is directly due to the radiative decay rate of the emitter.

The emitted dipole power when $z_0 < \lambda_1$ can be simulated numerically in a finite-difference time domain software (Lumerical). We again use a dipole perpendicular

and parallel to the surface, embedded in a bulk material with n = 2.4. A small 2 x 2 x 2 nm box was placed around the dipole to measure the transmitted power of the emitter. The power output of the box is normalized to the power the dipole would emit in a homogeneous medium ($P_0$). A 4 x 4 x 4 nm 1 nm-mesh was placed around the dipole. A fine mesh was also positioned around the interface of diamond and air. The resulting dipole power as a function of distance from surface is shown in figure A.3.



**Figure A.3:** Numerical calculation of the total emitted power of a dipole perpendicular (blue) and parallel (green) to the surface

The numerical results is similar to the analytical results presented in reference 47. A dipole perpendicularly oriented to the surface experiences a more drastic drop in emitter power. A dipole parallel to the surface increases in intensity from $z_0$ of 90 nm to 20 nm.
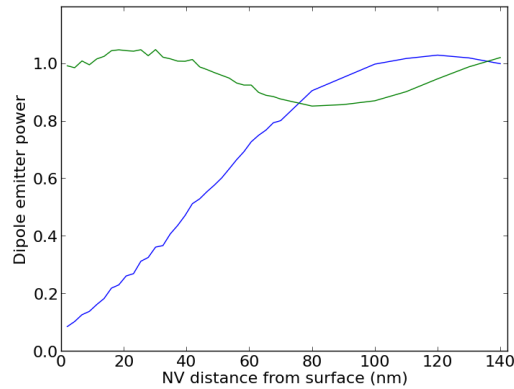
## A.2  COLLECTION OF DIPOLE RADIATION

In addition to the calculation of the total dipole power, we need to understand how effective our collection is. When a dipole is far from the interface ($z_0 > \lambda_1$), emission with angles higher than a critical angle experience total internally reflection back into medium 1. The critical angle is given by Snell's law $\theta_c = arcsin(n), n = \frac{n_2}{n_1}$. Hence, no transmission into medium 2 occurs beyond the critical angle. When the dipole distance is very small we can again represent the dipole field is as a combination of s- and p-polarized plane and evanescent waves. The reflection and refraction of both the plane and evanescent waves are then calculated the boundary.[46,45] The power radiated is calculated from the Fresnel transmittance. When n >1, the evanescent fields of the dipole can be refracted into the denser medium 2 and the collection efficiency changes with $z_0$. However, in our system, n <1, and this evanescent coupling does not occur. Therefore, the radiation patterns are independent of $z_0$. The calculated analytical solution, as provided by ref. 46,45 is shown in figure A.4a. The power output is shown as a function of angle (theta in fig A.1)

We simulated the far field projection of dipole emission in FDTD. We placed a near-field 2D monitor in air within 100 nm of the dipole, just above the interface. The measured electric fields were projected onto a hemispherical surface 1 meter from the surface. Figure A.4 compares the analytical and numerical simulations. Again, the two methods correspond to one another.
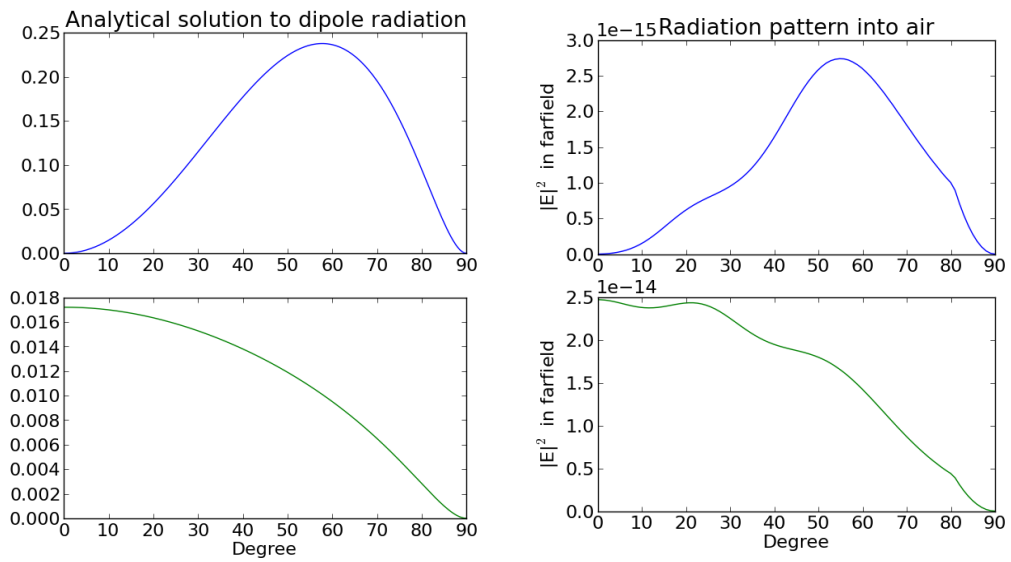
**Figure A.4:** Dipole radiation into air for a perpendicular (blue) and parallel (green) orientation to the surface. The analytical solution is plotted on the left. The simulation from FDTD software, with dipole situated 70 nm from the surface, is shown on the right.

# References

[1] Agraharam, S., Hess, D. W., Kohl, P. a., & Bidstrup Allen, S. a. (1999). Plasma chemistry in fluorocarbon film deposition from pentafluoroethane/argon mixtures. *Journal of Vacuum Science & Technology A: Vacuum, Surfaces, and Films*, 17(6), 3265.

[2] Babinec, T. M., Hausmann, B. J. M., Khan, M., Zhang, Y., Maze, J. R., Hemmer, P. R., & Loncar, M. (2010). A diamond nanowire single-photon source. *Nature nanotechnology*, 5(3), 195–9.

[3] Balasubramanian, G., Chan, I. Y., Kolesov, R., Al-Hmoud, M., Tisler, J., Shin, C., Kim, C., Wojcik, A., Hemmer, P. R., Krueger, A., Hanke, T., Leitenstorfer, A., Bratschitsch, R., Jelezko, F., & Wrachtrup, J. (2008). Nanoscale imaging magnetometry with diamond spins under ambient conditions. *Nature*, 455(7213), 648–51.

[4] Bradac, C., Gaebel, T., Naidoo, N., Sellars, M. J., Twamley, J., Brown, L. J., Barnard, a. S., Plakhotnik, T., Zvyagin, a. V., & Rabeau, J. R. (2010). Observation and control of blinking nitrogen-vacancy centres in discrete nanodiamonds. *Nature nanotechnology*, (April), 1–5.

[5] Bulu, I., Babinec, T., Hausmann, B., Choy, J. T., & Loncar, M. (2011). Plasmonic resonators for enhanced diamond NV- center single photon sources. *Optics Express*, 19(6), 402–406.

[6] Childress, L. & Hanson, R. (2013). Diamond NV centers for quantum computing and quantum networks. *MRS Bulletin*, 38(02), 134–138.

[7] Choy, J. T., Bulu, I., Hausmann, B. J. M., Janitz, E., Huang, I.-C., & Loncar, M. (2013). Spontaneous emission and collection efficiency enhancement of single emitters in diamond via plasmonic cavities and gratings. *Applied Physics Letters*, 103(16), 161101.

[8] Choy, J. T., Hausmann, B. J. M., Babinec, T. M., Bulu, I., Khan, M., Maletinsky, P., Yacoby, A., & Loncar, M. (2011). Enhanced single-photon emission from a diamond silver aperture. *Nature Photonics*, 5, 738.

[9] de Leon, N. P., Shields, B. J., Yu, C. L., Englund, D. E., Akimov, A. V., Lukin, M. D., & Park, H. (2012). Tailoring Light-Matter Interaction with a Nanoscale Plasmon Resonator. *Physical Review Letters*, 108(22), 226803.

[10] Deák, P., Aradi, B., Kaviani, M., Frauenheim, T., & Gali, A. (2014). Formation of NV centers in diamond: A theoretical study based on calculated transitions and migration of nitrogen and vacancy related defects. *Physical Review B*, 89(7), 075203.

[11] Denisenko, a., Romanyuk, A., Pietzka, C., Scharpf, J., & Kohn, E. (2010a). Surface damages in diamond by Ar/O2 plasma and their effect on the electrical and electrochemical characteristics of boron-doped layers. *Journal of Applied Physics*, 108(7), 074901.

[12] Denisenko, a., Romanyuk, a., Pietzka, C., Scharpf, J., & Kohn, E. (2010b). Surface structure and surface barrier characteristics of boron-doped diamond in electrolytes after CF4 plasma treatment in RF-barrel reactor. *Diamond and Related Materials*, 19(5-6), 423–427.

[13] Denisenko, A., Romanyuk, A., Pietzka, C., Scharpf, J., & Kohn, E. (2010c). Surface structure and surface barrier characteristics of boron-doped diamond in electrolytes after CF4 plasma treatment in RF-barrel reactor. *Diamond and Related Materials*, 19(5-6), 423–427.

[14] Doherty, M. W., Manson, N. B., Delaney, P., Jelezko, F., Wrachtrup, J., & Hollenberg, L. C. (2013). The nitrogen-vacancy colour centre in diamond. *Physics Reports*, 528(1), 1–45.

[15] Drexhage, K. H. (1970). Influence of a Dielectric Interface on Fluorescence Decay Time. *Journal of Luminescence*, 2, 693–701.

[16] Faraon, A., Barclay, P. E., Santori, C., Fu, K.-M. C., & Beausoleil, R. G. (2011). Resonant enhancement of the zero-phonon emission from a colour centre in a diamond cavity. *Nature Photonics*, 5(5), 301–305.

[17] Faraon, A., Santori, C., Huang, Z., Acosta, V. M., & Beausoleil, R. G. (2012). Coupling of Nitrogen-Vacancy Centers to Photonic Crystal Cavities in Monocrystalline Diamond. *Physical Review Letters*, 109(3), 033604.

102

[18] Fermi, E. (1997). *The Physics of Diamond.*

[19] Foord, J. S., Singh, N. K., Jackman, R. B., Gutierrez-Sosa, A., Proffitt, S., & Holt, K. B. (2001). Reactions of xenon difluoride and atomic hydrogen at chemical vapour deposited diamond surfaces. *Surface Science*, 488, 335–345.

[20] Fu, K.-M. C., Santori, C., Barclay, P. E., & Beausoleil, R. G. (2010). Conversion of neutral nitrogen-vacancy centers to negatively charged nitrogen-vacancy centers through selective oxidation. *Applied Physics Letters*, 96(12), 121907.

[21] Grotz, B., Hauf, M. V., Dankerl, M., Naydenov, B., Pezzagna, S., Meijer, J., Jelezko, F., Wrachtrup, J., Stutzmann, M., Reinhard, F., & Garrido, J. A. (2012). Charge state manipulation of qubits in diamond. *Nature communications*, 3, 729.

[22] Hadden, J. P., Harrison, J. P., Stanley-Clarke, a. C., Marseglia, L., Ho, Y.-L. D., Patton, B. R., OBrien, J. L., & Rarity, J. G. (2010). Strongly enhanced photon collection from diamond defect centers under microfabricated integrated solid immersion lenses. *Applied Physics Letters*, 97(24), 241901.

[23] Hall, L., Simpson, D., & Hollenberg, L. (2013). Nanoscale sensing and imaging in biology using the nitrogen-vacancy center in diamond. *MRS Bulletin*, 38(02), 162–167.

[24] Hanson, R. & Awschalom, D. D. (2008). Coherent manipulation of single spins in semiconductors. *Nature*, 453(7198), 1043–9.

[25] Hauf, M., Grotz, B., Naydenov, B., Dankerl, M., Pezzagna, S., Meijer, J., Jelezko, F., Wrachtrup, J., Stutzmann, M., Reinhard, F., & Garrido, J. (2011). Chemical control of the charge state of nitrogen-vacancy centers in diamond. *Physical Review B*, 83(8), 1–4.

[26] Hausmann, B. J., Khan, M., Zhang, Y., Babinec, T. M., Martinick, K., McCutcheon, M., Hemmer, P. R., & Lončar, M. (2010). Fabrication of diamond nanowires for quantum information processing applications. *Diamond and Related Materials*, 19(5-6), 621–629.

[27] Hong, S., Grinolds, M. S., Pham, L. M., Le Sage, D., Luan, L., Walsworth, R. L., & Yacoby, A. (2013). Nanoscale magnetometry with NV centers in diamond. *MRS Bulletin*, 38(02), 155–161.

[28] Hyuk Park, J., Nagpal, P., Oh, S.-H., & Norris, D. J. (2012). Improved dielectric functions in metallic films obtained via template stripping. *Applied Physics Letters*, 100(8), 081105.

[29] Inam, F. a., Grogan, M. D. W., Rollings, M., Gaebel, T., Say, J. M., Bradac, C., Birks, T. a., Wadsworth, W. J., Castelletto, S., Rabeau, J. R., & Steel, M. J. (2013). Emission and nonradiative decay of nanodiamond NV centers in a low refractive index environment. *ACS nano*, 7(5), 3833–43.

[30] Jelezko, F. & Wrachtrup, J. (2006). Single defect centres in diamond: A review. *Physica Status Solidi (a)*, 203(13), 3207–3225.

[31] Jinnai, B., Fukuda, S., Ohtake, H., & Samukawa, S. (2010). Prediction of UV spectra and UV-radiation damage in actual plasma etching processes using on-wafer monitoring technique. *Journal of Applied Physics*, 107(4), 043302.

[32] John, P. & Stoikou, M. D. (2011). Hydrogen plasma interaction with (100) diamond surfaces. *Physical chemistry chemical physics : PCCP*, 13(24), 11503–10.

[33] Kaviani, M., Deak, P., Aradi, B., Frauenheim, T., Chou, J.-p., & Gali, A. (2014). Proper Surface Termination for Luminescent Near-Surface NV Centers in Diamond. *Nano Letters*.

[34] Khan, R. U. a., Cann, B. L., Martineau, P. M., Samartseva, J., Freeth, J. J. P., Sibley, S. J., Hartland, C. B., Newton, M. E., Dhillon, H. K., & Twitchen, D. J. (2013). Colour-causing defects and their related optoelectronic transitions in single crystal CVD diamond. *Journal of physics. Condensed matter : an Institute of Physics journal*, 25(27), 275801.

[35] Kim, M., Mamin, H. J., Sherwood, M. H., Rettner, C. T., Frommer, J., & Rugar, D. (2014). Effect of oxygen plasma and thermal oxidation on shallow nitrogen-vacancy centers in diamond. *Applied Physics Letters*, 105(4), 042406.

[36] Krueger, A. (2011). Beyond the shine: recent progress in applications of nanodiamond. *Journal of Materials Chemistry*, 4, 12571–12578.

[37] Kruger, A., Liang, Y., Jarre, G., & Stegk, J. (2006). Surface functionalisation of detonation diamond suitable for biological applications. *Journal of Materials Chemistry*, 16(24), 2322.

[38] Kumar, S., Huck, A., & Andersen, U. L. (2013). Efficient coupling of a single diamond color center to propagating plasmonic gap modes. *Nano letters*, 13(3), 1221–5.

[39] Landstrass, M. I. & Ravi, K. V. (1989). Resistivity of chemical vapor deposited diamond films. *Applied Physics Letters*, 55(10), 975.

[40] Le Sage, D., Pham, L. M., Bar-Gill, N., Belthangady, C., Lukin, M. D., Yacoby, a., & Walsworth, R. L. (2012). Efficient photon detection from color centers in a diamond optical waveguide. *Physical Review B*, 85(12), 121202.

[41] Lee, J. C. (2013). *Fabrication and characterization of single-crystal diamond photonic cavities.* PhD thesis, Harvard University.

[42] Liu, N., Tang, M. L., Hentschel, M., Giessen, H., & Alivisatos, A. P. (2011). Nanoantenna-enhanced gas sensing in a single tailored nanofocus. *Nature Materials*, (May).

[43] Liu, T.-l., Russell, K. J., Cui, S., & Hu, E. L. (2014). Two-dimensional hybrid photonic / plasmonic crystal cavities. *Optics Express*, 22(7), 2242–2246.

[44] Loretz, M., Pezzagna, S., Meijer, J., & Degen, C. L. (2014). Nanoscale nuclear magnetic resonance with a 1.9-nm-deep nitrogen-vacancy sensor. *Applied Physics Letters*, 104(3), 033102.

[45] Lukosz, W. (1977). Light emission by magnetic and electric dipoles close to a plane dielectric interface . III . Radiation patterns of dipoles with arbitrary orientation. *Journal of the Optical Society of America*, 69(11), 1495.

[46] Lukosz, W. & Kunz, R. E. (1977a). Light emission by magnetic and electric dipoles close to a plane dielectric interface. II. Radiation patterns of perpendicular oriented dipoles. *Journal of the Optical Society of America*, 67(12), 1615–1619.

[47] Lukosz, W. & Kunz, R. E. (1977b). Light emission by magnetic and electric dipoles close to a plane interface . I . Total radiated power. *Journal of the Optical Society of America*, 67(12), 1607.

[48] Maier, F., Riedel, M., Mantel, B., Ristein, J., & Ley, L. (2000). Origin of surface conductivity in diamond. *Physical review letters*, 85(16), 3472–5.

[49] Maier, F., Ristein, J., & Ley, L. (2001). Electron affinity of plasma-hydrogenated and chemically oxidized diamond (100) surfaces. *Physical Review B*, 64(16), 1–7.

[50] Mamin, H. J., Kim, M., Sherwood, M. H., Rettner, C. T., Ohno, K., Awschalom, D. D., & Rugar, D. (2013). Nanoscale nuclear magnetic resonance with a nitrogen-vacancy spin sensor. *Science (New York, N.Y.)*, 339(6119), 557–60.

[51] Myers, B., Das, a., Dartiailh, M., Ohno, K., Awschalom, D., & a.C. Bleszynski Jayich (2014). Probing Surface Noise with Depth-Calibrated Spins in Diamond. *Physical Review Letters*, 113(2), 027602.

[52] Nagpal, P., Lindquist, N. C., Oh, S.-H., & Norris, D. J. (2009). Ultrasmooth patterned metals for plasmonics and metamaterials. *Science (New York, N.Y.)*, 325(5940), 594–7.

[53] Nebel, C. E., Rezek, B., Shin, D., & Watanabe, H. (2006). Surface electronic properties of H-terminated diamond in contact with adsorbates and electrolytes. *Physica Status Solidi (a)*, 203(13), 3273–3298.

[54] Novotny, L. & Hecht, B. (2006). *Principles of Nano-Optics*. Cambridge University Press.

[55] Oehrlein, G. S. (1989). Dry etching damage of silicon: A review. *Materials Science and Engineering: B*, 4(1-4), 441–450.

[56] Ofori-Okai, B. K., Pezzagna, S., Chang, K., Loretz, M., Schirhagl, R., Tao, Y., Moores, B. a., Groot-Berning, K., Meijer, J., & Degen, C. L. (2012). Spin properties of very shallow nitrogen vacancy defects in diamond. *Physical Review B*, 86(8), 081406.

[57] Ohashi, K., Rosskopf, T., Watanabe, H., Loretz, M., Tao, Y., Hauert, R., Tomizawa, S., Ishikawa, T., Shikata, S., Degen, C. L., & Itoh, K. M. (2013). Negatively Charged Nitrogen-Vacancy Centers in a 5 nm Thin 12C Diamond Film. *Nano*, 13, 4733–4738.

[58] Ohno, K., Joseph Heremans, F., Bassett, L. C., Myers, B. a., Toyli, D. M., Bleszynski Jayich, A. C., Palmstrom, C. J., & Awschalom, D. D. (2012). Engineering shallow spins in diamond with nitrogen delta-doping. *Applied Physics Letters*, 101(8), 082413.

[59] Osterkamp, C., Scharpf, J., Pezzagna, S., Meijer, J., Diemant, T., Jurgen Behm, R., Naydenov, B., & Jelezko, F. (2013). Increasing the creation yield of shallow single defects in diamond by surface plasma treatment. *Applied Physics Letters*, 103(19), 193118.

[60] Oulton, R. F., Sorger, V. J., Genov, D. a., Pile, D. F. P., & Zhang, X. (2008). A hybrid plasmonic waveguide for subwavelength confinement and long-range propagation. *Nature Photonics*, 2(8), 496–500.

[61] Oulton, R. F., Sorger, V. J., Zentgraf, T., Ma, R.-M., Gladden, C., Dai, L., Bartal, G., & Zhang, X. (2009). Plasmon lasers at deep subwavelength scale. *Nature*, 461(7264), 629–32.

[62] Pate, B. B. (1986). The Diamond Surface: Atomic and Electronic Structure. *Surface Science*, 165, 83–142.

[63] Petráková, V., Taylor, A., Kratochvílová, I., Fendrych, F., Vacík, J., Kučka, J., Štursa, J., Cígler, P., Ledvina, M., Fišerová, A., Kneppo, P., & Nesládek, M. (2012). Luminescence of Nanodiamond Driven by Atomic Functionalization: Towards Novel Detection Principles. *Advanced Functional Materials*, 22(4), 812–819.

[64] Pezzagna, S., Naydenov, B., Jelezko, F., Wrachtrup, J., & Meijer, J. (2010). Creation efficiency of nitrogen-vacancy centres in diamond. *New Journal of Physics*, 12(6), 065017.

[65] Popov, C., Kulisch, W., Bliznakov, S., Ceccone, G., Gilliland, D., Sirghi, L., & Rossi, F. (2008). Surface modification of nanocrystalline diamond/amorphous carbon composite films. *Diamond and Related Materials*, 17(7-10), 1229–1234.

[66] Riedrich-Möller, J., Kipfstuhl, L., Hepp, C., Neu, E., Pauly, C., Mücklich, F., Baur, A., Wandt, M., Wolff, S., Fischer, M., Gsell, S., Schreck, M., & Becher, C. (2012). One- and two-dimensional photonic crystal microcavities in single crystal diamond. *Nature nanotechnology*, 7(1), 69–74.

[67] Rietwyk, K. J., Wong, S. L., Cao, L., O'Donnell, K. M., Ley, L., Wee, a. T. S., & Pakes, C. I. (2013). Work function and electron affinity of the fluorine-terminated (100) diamond surface. *Applied Physics Letters*, 102(9), 091604.

[68] Ristein, J. (2006a). Surface science of diamond: Familiar and amazing. *Surface Science*, 600(18), 3677–3689.

[69] Ristein, J. (2006b). Surface transfer doping of diamond. *Journal of Physics D: Applied Physics*, 39(4), R71–R81.

[70] Rondin, L., Tetienne, J.-P., Hingant, T., Roch, J.-F., Maletinsky, P., & Jacques, V. (2014). Magnetometry with nitrogen-vacancy defects in diamond. *Reports on progress in physics. Physical Society (Great Britain)*, 77(5), 056503.

[71] Russell, K. J., Liu, T.-l., Cui, S., & Hu, E. L. (2012a). Large spontaneous emission enhancement in plasmonic nanocavities. *Nature Photonics*, 6(July), 2–5.

[72] Russell, K. J., Yeung, K. Y. M., & Hu, E. (2012b). Measuring the mode volume of plasmonic nanocavities using coupled optical emitters. *Physical Review B*, 85(24), 245445.

[73] Santori, C., Barclay, P. E., Fu, K.-M. C., Beausoleil, R. G., Spillane, S., & Fisch, M. (2010). Nanophotonics for quantum optics using nitrogen-vacancy centers in diamond. *Nanotechnology*, 21(27), 274008.

[74] Schietinger, S., Barth, M., Aichele, T., & Benson, O. (2009). Plasmon-enhanced single photon emission from a nanoassembled metal-diamond hybrid structure at room temperature. *Nano letters*, 9(4), 1694–8.

[75] Schirhagl, R., Chang, K., Loretz, M., & Degen, C. L. (2013). Nitrogen-Vacancy Centers in Diamond: Nanoscale Sensors for Physics and Biology. *Annual review of physical chemistry*, (November), 83–105.

[76] Sque, S., Jones, R., & Briddon, P. (2006). Structure, electronics, and interaction of hydrogen and oxygen on diamond surfaces. *Physical Review B*, 73(8), 1–15.

[77] Stacey, a., Karle, T. J., McGuinness, L. P., Gibson, B. C., Ganesan, K., Tomljenovic-Hanic, S., Greentree, a. D., Hoffman, a., Beausoleil, R. G., & Prawer, S. (2012). Depletion of nitrogen-vacancy color centers in diamond via hydrogen passivation. *Applied Physics Letters*, 100(7), 071902.

[78] Staudacher, T., Shi, F., Pezzagna, S., Meijer, J., Du, J., Meriles, C. a., Reinhard, F., & Wrachtrup, J. (2013). Nuclear magnetic resonance spectroscopy on a (5-nanometer)3 sample volume. *Science (New York, N.Y.)*, 339(6119), 561–3.

[79] Staudacher, T., Ziem, F., Haussler, L., Stohr, R., Steinert, S., Reinhard, F., Scharpf, J., Denisenko, A., & Wrachtrup, J. (2012). Enhancing the spin properties of shallow implanted nitrogen vacancy centers in diamond by epitaxial overgrowth. *Applied Physics Letters*, 101(21), 212401.

[80] Tanuma, S., Powell, C. J., & Penn, D. R. (2011). Calculations of electron inelastic mean free paths. IX. Data for 41 elemental solids over the 50 eV to 30 keV range. *Surface and Interface Analysis*, 43(3), 689–713.

[81] Tiwari, A. K., Goss, J. P., Briddon, P. R., Wright, N. G., Horsfall, A. B., Jones, R., Pinto, H., & Rayson, M. J. (2011). Calculated electron affinity and stability of halogen-terminated diamond. *Physical Review B*, 84(24), 1–9.

[82] van der Weide, J., Zhang, Z., Baumann, P. K., Wensell, M. G., Bernholc, J., & Nemanich, R. J. (1994). Negative-electron-affinity effects on the diamond (100) surface. *Physical Review B*, 50(8), 5803–5806.

[83] Vesseur, E. J. R. & Polman, A. (2011). Controlled spontaneous emission in plasmonic whispering gallery antennas. *Applied Physics Letters*, 99(23), 231112.

[84] Wheeler, V., Garces, N., Nyakiti, L., Myers-Ward, R., Jernigan, G., Culbertson, J., Eddy, C., & Kurt Gaskill, D. (2012). Fluorine functionalization of epitaxial graphene for uniform deposition of thin high-$\kappa$ dielectrics. *Carbon*, 50(6), 2307–2314.

[85] Wong, H. F., Green, D., Liu, T., Lishan, D., Bellis, M., Hu, E., Petroff, P., Holtz, P., & Merz, J. (1988). Investigation of reactive ion etching induced damage in GaAsAlGaAs quantum well structures. *Journal of Vacuum Science & Technology B: Microelectronics and Nanometer Structures*, 6(6), 1906.

[86] Xie, F. Y., Xie, W. G., Gong, L., Zhang, W. H., Chen, S. H., Zhang, Q. Z., & Chen, J. (2010). Surface characterization on graphitization of nanodiamond powder annealed in nitrogen ambient. *Surface and Interface Analysis*, 42(9), 1514–1518.